Alma Mater Studiorum

Università degli Studi di Bologna

DIPARTIMENTO DI FISICA E ASTRONOMIA

Dottorato di ricerca in Astronomia
Ciclo XXVI

Constraints on neutrino mass fraction using Redshift Space Distortions

Dottoranda:
Fernanda Petracca

Relatore:
Chiar.mo Prof. Lauro Moscardini

Co–Relatore:
Dott. Federico Marulli

Co–Relatore:
Chiar.mo Prof. Andrea Cimatti

Coordinatore:
Chiar.mo Prof. Lauro Moscardini

Esame finale anno 2014

Settore Concorsuale: 02/C1 – Astronomia, Astrofisica, Fisica della Terra e dei Pianeti
Settore Scientifico-Disciplinare: FIS/05 – Astronomia e Astrofisica

Contents

Abstract

Redshift Space Distortions (RSD) are an apparent anisotropy in the distribution of galaxies due to their peculiar motion at large scales. The peculiar velocities add to the Hubble flow and make these objects to appear squashed along the line of sight, leading to an increase of the clustering signal. On smaller scales, the non-linear motion of galaxies leads to what is called Fingers Of God, an elongation of the galaxy distribution which point to the observer.

These features are clearly imprinted in the correlation function of galaxies, a function which describes how these structures distribute around each other. RSD can be represented by a distortions parameter β, which is strictly related to the growth of cosmic structures. For this reason, measurements of RSD can be exploited to give constraints on the cosmological parameters, such us for example the neutrino mass.

Neutrinos are electrically neutral subatomic particles created by radioactive dacay or nuclear reaction such those that take palace in the Sun or when cosmic rays hit atoms. According to the standard model of particles, neutrinos are massless particles. There are three neutrino flavours, the electron, the muon and the tau neutrino, that only interact through the weak force, that is why they are so hard to detect. However, as theorised by Bruno Pontecorvo in 1957, neutrinos have been proven to undergo the mechanism of oscillations between flavour states. The discover has been made for the first time in late 1990's by the Super-Kamiokande experiment and implies that neutrino cannot be massless.

Neutrino oscillation experiments are sensitive the mass differences between the three eigenstates, but due to the very small cross-section of these particles, they can not measure directly their mass. Cosmology can assist the particle physics in the quest for neutrino masses. Indeed neutrinos leave a characteristic imprint on the large scale structure of the universe and different cosmological probes can be exploited to measure this parameter.

One of the most powerful tool to estimate neutrino mass is represented by RSD. Indeed, neutrino mass affects the growth of structure by reducing the matter power spectrum ampli-

tude below the free-streaming scale, introducing a scale dependence in the growth rate of density perturbations, a modification that reflects on the distortion parameters.

The aim of this thesis is to provide constraints on the accuracy with which neutrino mass can be estimated when expoiting measurements of RSD. In particular we want to describe how the error on the neutrino mass estimate depends on three fundamental parameters of a galaxy redshift survey: the density of the catalogue, the bias of the sample considered and the volume observed.

In doing this we make use of the BASICC Simulation, a simulation specifically designed to study the clustering properties of the universe. From this simulation we extract a series of dark matter halo catalogues, characterized by different value of bias, density and volume, and measure for each of them the correlation function. This mock data are analysed via a Markov Chain Monte Carlo procedure, in order to estimate the neutrino mass fraction, using the software package CosmoMC, which has been conveniently modified. Once we analysed all the catalogues, we are able to extract a fitting formula describing our measurements, which can be used to forecast the precision reachable in future surveys like Euclid, using this kind of observations.

The thesis is structured as follows:

- In Chapter 1 we review the basic concepts of the standard cosmological model, focusing out attention in particular on the growth of cosmic structures and the statistical tools used to describe their distribution in the universe.

- In Chapter 2 an overview of the RSD is presented. We show in detail the features imprinted by this effect in the correlation function of galaxies, describing how they can be modelled. We also show the link between theory and observations, reviewing some results from the recent literature.

- In Chapter 3 we describe the BASICC Simulation from which we extract the mock data, explaining how the correlation function is measured. Then we briefly present some technicalities related to the Markov Chain Monte Carlo likelihood analysis.

- In Chapter 4 we present the results on parameter estimation, with a detailed description of the methodology used. We also discuss all the issues related to the covariance matrix, which is used to assess the errors on the correlation function.

- In Chapter 5 we investigate how an incorrect use of the covariance matrix can affect parameter estimation, showing that the use of the full matrix can lead sometimes to the underestimation of the error, and that the smoothing procedure is not able to correct this issue.
- In Chapter 6 we show the measurements on neutrino mass fraction and present a new fitting function that describes the error dependence on bias, density and volume

In the Conclusion we finally summarize the results and discuss the open issues.

Chapter 1

The standard cosmological model

The accepted model that describes the Universe is the so called *Hot Big Bang* model, according to which the universe started to expand from an initial singularity, called indeed Big Bang, which implies infinite density and temperature. That's why this model has been called Hot. The existence of the cosmic microwave background radiation (CMB) with a black body spectrum, produced by freely moving photons after the decoupling between matter and radiation, which happened at redshift $z \simeq 10^3$, represents one of the most relevant evidences favouring the Hot Big Bang model.

This model is based on the cosmological principle, which states that, at least on large scale, the universe is homogeneous and isotropic, as confirmed by observations of CMB, whose photons coming from all the directions in the sky have the same temperature. On smaller scales instead we observe stars, galaxies and clusters, and this means that small deviations from homogeneity were present at early epochs and that they have grown through cosmic time under the effect of gravitational instability, giving rise to the structures we observe today.

Today the energy density of the universe is made up for $\sim 70\%$ by dark energy, for $\sim 25\%$ by dark matter and for $\sim 5\%$ by baryons, while radiation is almost negligible [57]. Dark energy and dark matter have never been observed directly. The presence of dark matter has been hypotesized at first to account for discrepancies between the mass of galaxies inferred from their gravitational effects and the mass of the luminous matter. Subsequently, many other observations have indicated the presence of dark matter in the universe, including gravitational lensing of background objects by galaxy clusters. The reasons which have led to the assumption of dark energy are the evidence of a spatially flat universe as derived from CMB anisotropy spectrum and the evidence of an accelerated

expansion of the universe, started in the recent past, as is evident from Type Ia Supernovae observations [56, 61, 62].

1.1 Einstein equations and the Friedmann-Robertson-Walker metric

The dynamics of the universe is described by the Einstein equations, which are in general complicated non-linear equations. However, they exhibit simple analytical solutions under the assumptions of homogeneity and isotropy.

Einstein equations take the form (hereafter we assume for simplicity $c = 1$):

$$G_{\mu\nu} = 8\pi G T_{\mu\nu} \ , \tag{1.1}$$

where

$$G_{\mu\nu} \equiv R_{\mu\nu} - \frac{1}{2} g_{\mu\nu} R \tag{1.2}$$

is the Einstein tensor, and $R_{\mu\nu}$ is the Ricci tensor, which describes the curvature of the space-time geometry and depends on the metric $\delta_{\mu\nu}$ and its derivatives, and $R = g_{\mu\nu} R^{\mu\nu}$ is the Ricci scalar. $T_{\mu\nu}$ is the energy-momentum tensor, which represents the source term of the Einstein equations and takes the form

$$T_{\mu\nu} = (\rho + P) u_\mu u_\nu + P g_{\mu\nu} \ , \tag{1.3}$$

where ρ and P are the energy density and the pressure of the fluid, respectively, and u_μ is the fluid four-velocity. If we consider an ideal perfect fluid, $T_{\mu\nu}$ takes the form $T^\nu_\mu = Diag(-\rho, P, P, P)$. The equation (1.1) tells us that the distribution of matter in the Universe, represented by the energy tensor $T_{\mu\nu}$, is strictly related to the space-time geometry, described by the Einstein tensor $G_{\mu\nu}$.

The Friedmann-Robertson-Walker (FRW) metric describes a 4-dimensional homogeneous and isotropic spacetime and is given by

$$ds^2 = g_{\mu\nu} dx^\mu dx^\nu = -dt^2 + a^2(t) \left[\frac{dr^2}{1 - Kr^2} + r^2 (d\theta^2 + \sin^2\theta d\phi^2) \right] \ , \tag{1.4}$$

where $a(t)$ is a scale factor (depending on cosmic time t) and K is the curvature, so that $K = +1, -1, 0$ correspond to closed, open and flat geometries. Under the assumptions of homogeneity and isotropy, which are valid at least on large scales, and in the presence of

a perfect fluid, the Einstein equations (1.1) reduce to two independent equations, known as Friedmann equations, which fully describe the evolution of the scale factor $a(t)$:

$$H^2 \equiv \left(\frac{\dot{a}}{a}\right)^2 = \frac{8\pi G\rho}{3} - \frac{K}{a^2} \tag{1.5}$$

$$\dot{H} = -4\pi G(\rho + P) + \frac{K}{a^2}\,, \tag{1.6}$$

where ρ and P denote the total energy density and pressure of all the species present in the universe at a given epoch. H is the *Hubble parameter* which describes the expansion rate of the universe. Its value at present epoch, H_0, is called the *Hubble constant*. It is commonly expressed as

$$H_0 = 100\,h\,\mathrm{km/s\,Mpc^{-1}} \tag{1.7}$$

and it is constrained to be $H_0 = 67.3 \pm 1.2$ km/s Mpc^{-1} according to latest Planck results [57].

Combining equations (1.5) and (1.6) we obtain

$$\frac{\ddot{a}}{a} = -\frac{4\pi G}{3}(\rho + 3P)\,. \tag{1.8}$$

Hence, for a perfect ordinary fluid, for which $\rho + 3P \geq 0$, the model described by Friedmann equations presents $\ddot{a} < 0$ and therefore describes a universe in decelerated expansion. An accelerated expansion occurs for $\rho + 3P < 0$. In any case the Friedmann equations imply $\ddot{a} \neq 0$ which means that the universe is expanding or contracting, but cannot be static.

If we define the critical density $\rho_{cr}(t) \equiv \frac{3H^2(t)}{8\pi G}$ as the density needed to obtain a spatially flat geometry, then the equation (1.5) can be rewritten in the form:

$$\sum_i \Omega_i(t) - 1 = \frac{K}{(aH)^2}\,, \tag{1.9}$$

where $\Omega_i(t) \equiv \rho_i(t)/\rho_{cr}(t)$ is the dimensionless density parameter for each component of the universe. This equation stresses again the fact that the total energy distribution determines the spatial geometry, as stated by Einstein when he formulated the theory of General Relativity. In particular we can distinguish three cases:

$$\sum_i \Omega_i > 1 \quad \text{or} \quad \sum_{\mathrm{i}} \rho_{\mathrm{i}} > \rho_{\mathrm{c}} \quad \rightarrow \quad K = +1 \quad \text{closed}\,, \tag{1.10}$$

$$\sum_i \Omega_i = 1 \quad \text{or} \quad \sum_{\mathrm{i}} \rho_{\mathrm{i}} = \rho_{\mathrm{c}} \quad \rightarrow \quad K = 0 \quad \text{flat}\,, \tag{1.11}$$

$$\sum_i \Omega_i < 1 \quad \text{or} \quad \sum_{\mathrm{i}} \rho_{\mathrm{i}} < \rho_{\mathrm{c}} \quad \rightarrow \quad K = -1 \quad \text{open}\,. \tag{1.12}$$

These three different models, following back in time the evolution of the scale factor, predict an initial singularity in which $a(0) = 0$, the *Big Bang*. For relativistic particles, non-relativistic matter, dark energy and curvature, we have:

$$\Omega_{0r} = \frac{8\pi G\rho_{0r}}{3H_0},\ \Omega_{0m} = \frac{8\pi G\rho_{0m}}{3H_0}, \Omega_{0DE} = \frac{8\pi G\rho_{0DE}}{3H_0},\ \Omega_{0K} = -\frac{K}{(a_0H_0)^2}, \quad (1.13)$$

where the subscript 0 denotes the values at present epoch. With these parameters, eq (1.9) can be rewritten as:

$$H^2(t) = H_0^2\left[(1+z)^4\Omega_{0r} + (1+z)^3\Omega_{0m} + (1+z)^2\Omega_{0K} + \Omega_{0DE}\right], \quad (1.14)$$

which allows to obtain the Hubble parameter at a given time, or redshift, starting from the present value of parameters.

1.2 Dark Energy

Let us consider the case in which the universe is dominated by a single component with an equation of state defined by

$$w \equiv \frac{P}{\rho}. \quad (1.15)$$

If w is a constant, one can analitically find the evolution of ρ and a for the flat universe. Solving the Friedmann equations, in this case we obtain the following solutions:

$$\rho \propto a^{-3(1+w)},\ a \propto (t-t_i)^{2/(3(1+w))}, \quad (1.16)$$

where t_i is a constant. Since from statistical mechanics we know that radiation has the equation of state $w = 1/3$, it follows that the cosmic evolution during the radiation-dominated epoch is given by $\rho \propto a^{-4}$ and $a \propto (t-t_i)^{1/2}$. Non-relativistic matter corresponds to the case with a negligible pressure, i.e. $w \simeq 0$. Then the evolution during the matter-dominated era is given by $\rho \propto a^{-3}$ and $a \propto (t-t_i)^{2/3}$.

These two kinds of fluid, according to equation (1.6), produce a decelerated expansion. However, the observations accumulated since 1998, coming from Supernovae Ia, CMB anisotropy and large scale structure, report that the universe is actually in a phase of accelerated expansion, which cannot be driven by ordinary or dark matter, neither radiation. Moreover these observations tell us that the universe is spatially flat. The sum of density parameters of baryonic matter, dark matter and radiation is smaller than unity and hence it is not sufficient to explain the flatness of the universe.

These two facts can be explained if we introduce an extra component, called dark energy, which is able to give an important contribution to the total energy density of the universe and so to justify its flat geometry. What we know about this component is that it causes the accelerated expansion and hence it needs to have a strong negative pressure in order to break the condition $\rho + 3P \geq 0$. This gives us a first clue on the nature of dark energy since its equation of state parameter needs to satisfy the condition $w < -1/3$.

The first description for this component is represented by the *cosmological constant*, originally introduced by Einstein in 1917 in order to obtain a static solution for his equations and then discarded after the discovery of the universe expansion by Hubble. While Einstein introduced his cosmological term as a modification to the curvature side of the field equation, it is now common to interpret Λ as a new energy component, constant in space and time. For a component whose energy density remains constant as the universe expands, the first law of thermodynamics implies negative pressure since $-PdV = dU = \rho dV$ and then $P = -\rho$. Hence the cosmological constant correspond to a fluid with a constant equation of state $w = -1$. From the particle physics point of view the cosmological constant is supposed to be the energy density of the vacuum. However the ratio between the theoretical and observed values of this energy density gives a discrepancy of 120 orders of magnitude, which is known as the *Cosmological Constant Problem*. The other basic puzzle concerning a cosmological constant is the so called *coincidence problem*, which can be expressed in this way: matter density scales as $a(t)^3$ while the vacuum energy density is constant, so why does it happen that the two components have the same order of magnitude just today?

Current observations can say relatively little about the possibility of a time evolution of w and so we can broaden our horizons and consider a situation in which the equation of state of dark energy can change with time. Such models are known as dynamical dark energy models and, contrary to the cosmological constant, can be characterized by a time varying and spatially inhomogeneous dark energy component, which can develop fluctuations relevant in the growth of perturbations and can leave a characteristic signature in the cosmic microwave background.

In this framework, a straightforward alternative to a cosmological constant is represented by models that introduce a new scalar field with negative pressure whose energy density changes with time. Many of these models are know as *Quintessence models* [10, 79, 1].

A canonical scalar field ϕ with potential $V(\phi)$ has energy density and pressure

$$\rho_\phi = \frac{1}{2}\dot{\phi}^2 + V(\phi) \tag{1.17}$$

$$P_\phi = \frac{1}{2}\dot{\phi}^2 - V(\phi)\,, \tag{1.18}$$

so, if the kinetic term is subdominant, then $P_\phi \approx -\rho_\phi$. In general the equation of state for the field ϕ ranges in the region $-1 \leq w_\phi \leq 1$. Some forms of $V(\phi)$ allow "tracker" solutions in which late-time evolution of ϕ is insensitive to the initial conditions [71], and a subset of these allows ρ_ϕ to mimic the behaviour of the dominant component until it starts to dominate at present epoch, alleviating the coincidence problem.

Scalar-tensor theories [24, 26] represent a framework to interpret the additional scalar field as the one which determines the Newton gravitational constant. This class of theories aims at modifying General Relativity itself rather than to add a new energy component. The prototype of these theories has been introduced by Brans and Dicke [8] in order to explain long range forces, such as gravity, in term of a scalar field. In general, the Ricci scalar is replaced in the gravitational action with some higher order function $f(R)$ which represents a non-minimal coupling term between the scalar field and the Ricci scalar. This function introduces new terms in the perturbed Einstein equations, which can leave a prominent sign in observations of the integrated Sachs-Wolfe effect or the lensing potential. Moreover, modification to General Relativity can alter the relation between the expansion history and the growth of matter clustering, and searching for mismatches between observational probes of expansion and observational probes of structure growth is one generic approach to seek signatures of modified gravity.

These are just few examples of the models proposed in the last years to describe dark energy and the challenge for theoretical physicists is still open, especially in view of the upcoming ESA space mission Euclid [46, 3], which will measure shapes and redshifts of galaxies and clusters of galaxies out to redshift ~ 2, covering the entire period in which dark energy plays an important role in accelerating expansion.

1.3 Cosmic Inflation

Despite al the successes of the Hot Big Bang model, there remain some unsatisfactory aspects, that can be explained introducing a phase of accelerated expansion in the early

stage of the universe, named *inflation*.

The *horizon problem* is one of the most important problems of the Hot Big Bang model and is related to the connection between different regions of the universe. The cosmological horizon is defined as the distance that the light can travel starting from the initial time (the Big Bang) and represents the scale for two events being causally connected at a given time t:

$$R_H(t) = \int_0^t \frac{dt'}{a(t')} \,. \tag{1.19}$$

The crucial ingredient is that the universe has only a finite age and so even light can only have travelled a finite distance by any given time.

One of the most relevant properties of the microwave background is that it is almost isotropic, that is, light seen from all directions in the sky possesses almost the same temperature of 2.725 K. This observation is naturally explained if different regions of the sky have been able to interact and move towards thermal equilibrium. Unfortunately, the light we see from the opposite side of the sky has been travelling toward us since decoupling, therefore there has not been enough time for these two regions to interact in any way and so it is not possible for them to have the same temperature. The final twist in the tail, which elevates this to a problem of extreme relevance, is that actually the microwave background is not perfectly isotropic but instead exhibits small fluctuations, of the order of one part in 10^5. For the same reason that one cannot thermalize separate regions, one can not create irregularities like the ones seen in the CMB.

Another important problem is the so called *flatness problem*. From equation (1.9) it is possible to see that if the universe is flat, then it remains flat for all the time. Otherwise the density parameter can evolve. This is due to the fact that the quantity aH is a decreasing function of time, and then $|1-\Omega| \propto t^{2/3}$ in a matter dominated universe ,and $|1-\Omega| \propto t$ in a radiation dominated universe. We know observationally that, at present, Ω_0 is not far from unity, which implies that at much earlier times, it must have been very close to 1, for example $|1-\Omega| \leq 10^{-60}$ when the universe was 1 second old. The flatness problem states that such fine tuned initial conditions seem extremely unlikely. Almost all initial conditions lead either to a closed universe that recollapses almost immediately, or to an open universe that very quickly enters the curvature dominated regime.

These are only two of the theoretical problems which afflict the Hot Big Bang model. Another one is, for example, the one related to the magnetic monopoles. Magnetic monopoles are predicted by unification theory such as GUT, during the primordial phases of the expansion of the universe. These monopoles would have a density parameter of the order $\Omega_0^{monopole} \simeq 10^{16}$. Therefore, together with the problem of having never been observed, they are strongly incompatible with the observed value of Ω_0.

All these problems find their solution if we hypothesize the existence of a primordial phase of accelerated expansion of the universe. During this phase, the horizon grows more slowly with respect to the scale factor, implying the exit from the horizon of regions which were causally connected. So it is possible to explain the isotropy of the cosmic radiation, since regions which appear non-connected at the time of last scattering, could have been causally connected during the phase before inflation.

At the same time, the accelerated expansion can explain the flatness problem, because it dilutes the curvature density reducing the difference between the density parameter and unity.

1.4 Cosmological perturbations

The true merit of inflation, however, is that it provides a theory of inhomogeneities in the universe, which may explain the observed structures. These inhomogeneities arise from quantum fluctuations in the inflation field about its vacuum state. The theory of structure formation, based on gravitational instability, describes how primordially generated fluctuations in matter and radiation grow into galaxies and clusters of galaxies due to self gravity.

CMB observations indicate that the anisotropies at the epoch of decoupling were rather small (one part in 10^5), implying that their amplitudes were even smaller at earlier epochs. This suggests that the generation and the evolution of the perturbations (until structures begin to form, late in the matter dominated epoch), can be studied using linear perturbation theory.

Gravitational fluctuations can be described through the metric

$$g_{\mu\nu} = g^{(0)}_{\mu\nu} + g^{(1)}_{\mu\nu} \ , \tag{1.20}$$

where $g^{(0)}_{\mu\nu}$ can be identified with the usual Friedmann-Robertson-Walker metric, while $g^{(1)}_{\mu\nu}$

is its small perturbation. So the perturbed FRW metric can be written in this general form:

$$ds^2 = -(1+2\Psi)dt^2 + a^2(t)w_i dt dx^i + a^2(t)[(1-2\Phi)\delta_{ij} + \chi_{ij}]dx^i dx^j \,, \tag{1.21}$$

where the functions Φ e Ψ, w_i and χ_{ij} represent scalar, vector and tensor modes of metric perturbations about FRW spacetime, respectively, and are assumed to be small compared to unity.

The perturbed Einstein equations in Newtonian gauge are [51]:

$$\delta G_{\mu\nu} = \delta R_{\mu\nu} - \frac{1}{2}\delta g_{\mu\nu} R - \frac{1}{2} g_{\mu\nu}\delta R = 8\pi G \delta T_{\mu\nu} \,. \tag{1.22}$$

Making all the terms explicit in Fourier space we obtain:

$$3H\left(H\Psi + \dot{\Phi}\right) \;+\; \frac{k^2}{a^2}\Phi = -4\pi G \sum_\alpha \delta\rho_\alpha \,, \tag{1.23}$$

$$k^2\left(H\Psi + \dot{\Phi}\right) \;=\; 4\pi G a \sum_\alpha (\rho_\alpha + P_\alpha)\,\theta \,, \tag{1.24}$$

$$\ddot{\Phi} + 3H\dot{\Phi} + 2\dot{H}\Psi + 3H^2\Psi + H\dot{\Psi} + \frac{k^2}{3a^2}(\Phi - \Psi) = 4\pi G \sum_\alpha \delta P_\alpha \,, \tag{1.25}$$

$$k^2(\Psi - \Phi) \;=\; 12\pi G \sum_\alpha (\rho_\alpha + P_\alpha)\,\sigma_\alpha \,. \tag{1.26}$$

Here the sums are taken all over the fluid components α, and θ is the divergence of the fluid velocity.

The perturbed part of the energy-momentum conservation equations instead can be written as:

$$\dot{\tilde{\delta}} \;=\; -(1+w)\left(\frac{\theta}{\alpha} - 3\dot{\Phi}\right) - 3H\left(\frac{\delta P}{\delta\rho} - w\right)\tilde{\delta} \,, \tag{1.27}$$

$$\dot{\theta} \;=\; -H(1-3w)\theta - \frac{\dot{w}}{1+w}\theta + \frac{\delta P/\delta\rho}{1+w}\frac{k^2}{a}\tilde{\delta} - \frac{k^2}{a}\sigma + \frac{k^2}{a}\Psi \,, \tag{1.28}$$

where $w \equiv P/\rho$ describes the fluid equation of state, $\tilde{\delta}$ is the density contrast defined as $\tilde{\delta} \equiv \delta\rho/\rho$ and σ is the anisotropic stress.

We can define a gauge invariant density perturbation in this way:

$$\delta \equiv \tilde{\delta} + 3H(1+w)\frac{a\theta}{k^2} = \tilde{\delta} + 3H(1+w)v \,, \tag{1.29}$$

where $a\theta/k^2 = v$. So we can rewrite the equation (1.23) with the new definition of comoving velocity:

$$H\Psi + \dot{\Phi} = 4\pi G \sum_\alpha (\rho_\alpha + P_\alpha) v_\alpha \,, \tag{1.30}$$

while the perturbed conservation equations become:

$$\dot{\delta} = -(1+w)\frac{k^2}{a^2}v + 3(1+w)(\Phi + Hv)^{\cdot} - 3H\left(\frac{\delta P}{\delta\rho} - w\right)\delta\,, \tag{1.31}$$

$$\dot{v} = 3Hwv - \frac{\dot{w}}{1+w}v + \frac{\delta P}{\rho(1+w)} - \sigma + \Psi\,. \tag{1.32}$$

Combining the latter equations we obtain a general evolution equation for the comoving matter density contrast:

$$\ddot{\delta} + 2H\dot{\delta} + \frac{k^2}{a^2}\Phi = 3\ddot{B} + 6H\dot{B}\,, \tag{1.33}$$

where $B \equiv \Phi + Hv$. From this equation it is possible to derive the evolution equations for matter perturbations in different cases, for example for different kinds of fluid or in presence of dark energy.

Let us consider a fluid which is pressureless ($w = 0$) in absence of perturbations, but with a small sound speed $c_s^2 = \frac{\delta P}{\delta\rho}$. In this case, and in sub-horizon approximation, the evolution equation takes this simple form:

$$\ddot{\delta} + 2H\dot{\delta} + \left(\frac{k^2}{a^2}c_s^2 - \frac{3}{2}H^2\right)\delta = 0. \tag{1.34}$$

This equation tells us that perturbations can grow if $\frac{k^2}{a^2}c_s^2 - \frac{3}{2}H^2 > 0$. This is verified if the physical wavelength of perturbations $\lambda_p = \frac{2\pi a}{k}$ is smaller than the Jeans length:

$$\lambda_J = c_s^2\sqrt{\frac{\pi}{G\rho}}. \tag{1.35}$$

For scales smaller than λ_J the perturbations undergo damped oscillations. For cold dark matter c_s represents the velocity dispersion, since cold dark matter is non-collisional, hence pressure is negligible and so it is the sound speed. This velocity opposes to gravity and the motion of the different elements of the fluid cancels out the perturbations. For the photons we have $c_s = c/\sqrt{3}$, so that $\lambda_J \simeq H^{-1}$. Hence the growth of perturbations is prevented on all scales smaller that the Hubble radius H^{-1}. For baryons, the sound speed is comparable to the photon velocity before the decoupling epoch, so their perturbations are damped out. When $c_s k << H$ the perturbations grow freely because gravity overcomes the pressure: this is the regime of gravitational instability. The equation becomes:

$$\ddot{\delta} + 2H\dot{\delta} - \frac{3}{2}H^2\delta = 0\,, \tag{1.36}$$

which has a growing and a decaying mode solution: $\delta(\mathbf{x}, t) = A(x)D_+(t) + B(x)D_-(t)$, where the factors $A(x)$ and $B(x)$ are fixed by the initial conditions. The decaying solutions become soon negligible with respect to the growing ones and therefore can be neglected.

The solution can be written as a function of the growing mode only as:

$$\delta(\mathbf{x}, t) = \delta(\mathbf{x}, t_i) \cdot \frac{D(t)}{D(t_i)} \,, \tag{1.37}$$

where t_i is an arbitrarily chosen initial time and $D(t) \propto a(t) \propto t^{2/3}$ (for sake of simplicity we omit hereafter the subscript $+$). The *linear growth function* $D(t)$ obeys the differential equation

$$\ddot{D}(t) + 2H(z)\dot{D}(t) - \frac{3}{2}\Omega_m H_0^2 (1+z)^3 D(t) = 0. \tag{1.38}$$

The solution to this equation can only be written in integral form as a function of $H(z)$ and thus for a specific dark energy models. However, to a very good approximation the logarithmic *growth rate* of linear perturbation in General Relativity, defined as

$$f(z) \equiv \frac{d \ln D}{d \ln a} \,, \tag{1.39}$$

is an analytic function of Ω_m approximated as a power law $f(\Omega_m) \approx \Omega_m(z)^\gamma$, where γ is the *linear growth factor*. Integrating this equation yields

$$\frac{D(z)}{D(z=0)} \approx \exp\left[-\int_0^z \frac{dz'}{1+z'} \Omega_m(z')^\gamma \right]. \tag{1.40}$$

Linder [50] shows that this equation is accurate to better than 0.5% for a wide variety of dark energy models if one adopts

$$\gamma = 0.55 + 0.05[1 + w(z=1)]. \tag{1.41}$$

Note that for a dark energy model with an evolving density parameter, $\Omega_m(z)$ is lower with respect to a cosmological constant case, therefore the ratio $D(z)/D(z=0)$ is higher, which means that there has been less growth of structure between redshift z and the present day because matter has a smaller contribution to the total density over that time. Thus it is clear that investigating the behaviour of the growth rate with redshift can help us to shed light upon the nature of dark energy.

1.5 Properties of the density perturbation field

The linear perturbation theory is a powerful tool that can be used to make predictions about large scale structure. Even though the evolution of perturbations in the linear regime is known, the non-linear evolution leading to the formation of small scale structures is not

so well understood. That is why computer simulations are usually used: given an initial density perturbation $\delta(\mathbf{x}, t_0)$ at some time t_0, we can compute in principle the final mass distribution, including the distribution of structures like galaxies.

With theoretical results in our hands, we have to compare them with observations. Of course it is meaningless to hope that theory will be able to produce the properties of a particular galaxy located at a particular coordinate $\mathbf{x}$; or in general we do not expect the theory to predict the density contrast at any specified location, since this prediction requires the knowledge of the fine-tuned initial conditions $\delta(\mathbf{x}, t_i)$. Thus, instead of predicting the exact mass distribution of our universe, we shall predict the average, statistical properties of the mass distribution. In doing this it is necessary to invoke the mathematical concept of random fields and their properties.

A density perturbation, evaluated at some instant in a certain coordinate in space, is defined as

$$\delta(\mathbf{x}) \equiv \frac{\rho(\mathbf{x}) - \bar{\rho}}{\bar{\rho}} \,, \tag{1.42}$$

where $\bar{\rho}$ is the mean density of the universe. We can say that $\delta(\mathbf{x})$ is associated to what is called a *random field*, that is, for each point in space a set of functions $\delta_n(\mathbf{x})$ exists, each coming with a probability P_n. The set of function $\delta_n(\mathbf{x})$ is referred to as the *ensamble*, and each individual function is called a *realization* of the ensamble. This means that the density field that we observe is one of the possible realizations of the field.

Even though our present universe is not stricly homogeneous it does appear to be *statistically* homogeneous, in the sense that we can recover similar properties at any position. Hence it is possible to make a fundamental assumption about the density fluctuations field, saying that the field $\delta(\mathbf{x})$ consitutes a homogeneous and isotropic random field, which is just an extension of the Cosmological Principle. In other words, we can assume that the probability of each realization is supposed to be invariant under translations and rotations. Translation invariance (homogeneity) means that the probability attached to a realization $\delta_n(\mathbf{x})$ is the same as the one of the realization $\delta_n(\mathbf{x} + \mathbf{X})$, for each fixed $\mathbf{X}$. Rotational invariance (isotropy) means that the probability of a realization $\delta_n(\mathbf{x})$ is the same as the probability of the realization $\delta_n(\tilde{\mathbf{x}})$ where $\tilde{\mathbf{x}}$ are rotated coordinates.

The Fourier expansion is a powerful tool for analysing stochastic properties, so we want to introduce some definition in the Fourier formalism. A generic perturbation, evaluated at

some particular time, in a certain coordinate in space can be written as:

$$\delta(\mathbf{x}) = \frac{1}{(2\pi)^3} \int \delta(\mathbf{k}) \exp^{i\mathbf{k}\cdot\mathbf{x}} d^3k \,, \tag{1.43}$$

while its inverse is

$$\delta(\mathbf{k}) = \int \delta(\mathbf{x}) \exp^{-i\mathbf{k}\cdot\mathbf{x}} d^3x. \tag{1.44}$$

Notice that $\delta(\mathbf{x})$ is an adimensional quantity, while $\delta(\mathbf{k})$ has the dimension of a volume.

According to the theory of structure formation, the density fluctuations on scale $\mathbf{k}$ form a Gaussian scalar field. A Gaussian random field may be defined as one whose Fourier modes have no correlation except for the reality condition $g(-\mathbf{k}) = g^*(\mathbf{k})$. Gaussianity means that drawing these modes randomly from the ensemble, each of them has an independent probability distribution. But the central limit theorem states, under very general conditions, that the sum of uncorrelated quantities has gaussian probability distribution independently of the probability distribution of the original quantities. We conclude that, for a Gaussian random field, the probability distribution of $\delta(\mathbf{x})$ at a given point is Gaussian. A Gaussian distribution is univocally described by its mean and its variance. Hence, since $\delta(\mathbf{x})$ has zero mean, we just need its variance in order to completely describe it.

1.6 Correlation function and power spectrum

The most basic statistic that can be constructed from the overdensity field is the *correlation function*:

$$\xi(r) \equiv \langle \delta(\mathbf{x})\delta(\mathbf{x}+\mathbf{r}) \rangle \ , \tag{1.45}$$

where angular brackets indicate an average over a normalization volume. The correlation function $\xi(r)$ is the mean overdensity of neighbour around a random position. The assumption that the density field is statistically homogeneous and isotropic makes $\xi(r)$ a function only of the scalar separation r of two points, and not of their overall location or orientation.

Using the Fourier expansion of $\delta(\mathbf{x})$ in the equation (1.45), the correlation function can be expressed as:

$$\xi(r) = \frac{1}{(2\pi)^3} \int \langle |\delta(k)|^2 \rangle \exp^{-i\mathbf{k}\cdot\mathbf{x}} d^3k \,. \tag{1.46}$$

By definition $\langle |\delta(k)|^2 \rangle$ is the *power spectrum* of modes of wavenumber k, then this equation tells us that the correlation function is the Fourier transform of the power spectrum, which

is usually denoted as $P(k)$ and is mathematically defined as

$$\langle \delta(\mathbf{k})\delta(\mathbf{k}')\rangle \equiv (2\pi)^3 P(k)\delta_D(\mathbf{k}-\mathbf{k}') \,, \tag{1.47}$$

where $\delta_D(\mathbf{k}-\mathbf{k}')$ is the Dirac delta function. Again, thanks to the isotropy of the density perturbation field, the power spectrum depends only on the module of the wavenumber $\mathbf{k}$. Hence the angular part of the integral (1.46) can be performed immediately, obtaining:

$$\xi(r) = \frac{1}{2\pi^2}\int k^2 P(k)\frac{\sin kr}{kr}dk \,. \tag{1.48}$$

The physical meaning of the power spectrum is the following: $P(k)$ is a measure of the power of fluctuations on scale k, that is, it tells us how much a perturbation with wavenumber k contributes in forming a perturbation $\delta(\mathbf{x})$ in configuration space. To clarify this concept we can consider the simple example in which $\delta(\mathbf{x})$ is made up by a single plane wave of wavenumber k. Recalling equation (1.47) we can see that its Fourier transform is zero everywhere except in k and $P(k)$ will be a Dirac delta function. Then in the generic case $P(k)$ will have a higher value for those wavenumber k which contribute the most to $\delta(\mathbf{x})$.

Although the mean value of the perturbation $\delta(\mathbf{x})$ across the statistical ensamble is zero by definition, its variance σ^2 is not. From the definition introduced before we can define the variance as

$$\sigma^2 \equiv \langle \delta^2(\mathbf{x})\rangle = \frac{1}{2\pi^2}\int_0^\infty P(k)k^2 dk \,. \tag{1.49}$$

The variance does not depend on spatial position but on time, because the perturbation amplitudes $\delta(\mathbf{k})$ evolve. The quantity σ^2 therefore tells us about the amplitude of perturbations, but it does not carry information about their spatial structure.

Simple inflationary theories predict that just after inflation the matter power spectrum would have been a simple power law $P(k) \propto k^n$, where the exponent n is usually called *spectral index*. This exponent needs not to be constant over the entire range of wavenumbers: the convergence of the integral (1.49) requires that $n > -3$ for $k \to \infty$ and $n < -3$ for $k \to 0$. The power spectrum has then evolved in shape as the Universe has gone through various phases in its evolution, and at the present day shows a peak whose position corresponds to the Jeans length at matter-radiation equality.

1.7 Bias

The variance of the field characterizes the mean amplitude of perturbations in a specific point in space. Of course what we observe is not the fluctuation field but the distribution of galaxies. In order to compare observations with theory we need to make some assumptions about how galaxies are distributed with respect to the underlying matter distribution. To do this we can introduce the concept of *bias*. If galaxies were unbiased tracers of matter, then they would satisfy the relation $\delta_g = \delta_m$, by definition. That some bias exists, at least in some galaxy population, follows from the fact that galaxies selected in different ways have correlation function with different amplitudes. The simplest model of bias postulates that the galaxy overdensity δ_g is linearly biased by a constant factor, the linear bias factor b, relative to matter overdensity, so that:

$$\delta_g = b\delta_m \ . \tag{1.50}$$

Of course it does not make sense to define the galaxy overdensity in a certain point, as we do with matter overdensity. Instead we usually ask how many galaxies we can find in a certain volume in space. Then, the next step in comparing theory and observations is to average the matter overdensity over a volume and to compare it with the number of galaxies in the same volume. From this point of view, the bias can be rewritten in a more statistical way as:

$$b = \frac{\sigma_g}{\sigma_m} \ , \tag{1.51}$$

where σ_g and σ_m are the variances of galaxy distribution and matter, respectively, integrated over a sphere of radius $8h^{-1}\mathrm{Mpc}$, basically smoothing out all the non-linear effects below this scale.

Chapter 2

Redshift space distortions

Redshift Space Distortions (hereafter RSD) are, as the name says, distortions in the distribution of galaxies due to their peculiar velocities. The distribution of galaxies that we observe in a sky survey is not the real picture. In redshift space we observe a clustering pattern which is different from the one in real space because galaxy redshifts are altered from Hubble flow prediction by their peculiar velocities. So, when we compute galaxy distances from their redshift assuming that the total velocity relative to us comes only from the Hubble flow we obtain a distorted, redshift space, density field. This effect can be quantified helping us to constrain some cosmological parameters.

2.1 How RSD look like

In the 1920s Hubble discovered that the observed wavelength λ_0 of absorption lines of distant galaxies is larger than the wavelength in the rest frame. This is due to the fact that the wavelength is stretched in proportion to the scale factor in an expanding universe. This effect can be quantified introducing a new quantity called *redshift*:

$$z \equiv \frac{\lambda_0}{\lambda} - 1 = \frac{a_0}{a} - 1 \tag{2.1}$$

where subscript 0 indicates the quantity at the present epoch. In particular $a_0 = 1$ and then $z_0 = 0$, and as we go back to the past, z becomes larger and larger. As long as the recessional velocity v of an object is much smaller than the speed of light c we have $\lambda_0 \simeq (1 + v/c)\lambda$ according to the Doppler effect, which gives

$$z \simeq v/c. \tag{2.2}$$

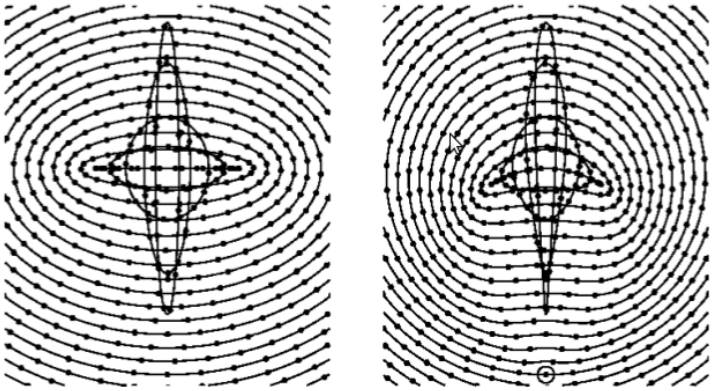

Figure 2.1: A spherical overdensity appears distorted by peculiar velocities when observed in redshift space. On the left, the overdensity is far from the observer and the distortions are effectively plane-parallel. On the right, the overdensity is near the observer (large dot), and the large scale distortions appear kidney-shaped while the finger-of-god is sharpened on the end pointing at the observer. [30]

Hubble's law states that the recession velocity of a galaxy is proportional to its distance d:

$$cz = H_0 d. \tag{2.3}$$

This velocity can be measured accurately from the redshift z of the galaxy spectrum, more easily and accurately than its true distance d. Hubble's law however is not accurate. Galaxies have peculiar velocities v relative to the Hubble's flow, so it is necessary to distinguish between a galaxy's redshift distance $s \equiv cz$ and its true distance $r \equiv H_0 d$, both expressed in velocity units. Then the redshift distance s of a galaxy differs from the true distance r by its peculiar velocity v along the line of sight:

$$s = r + v. \tag{2.4}$$

The peculiar velocities of galaxies thus cause them to appear displaced along the line of sight in redshift space. These displacement lead to RSD in the pattern of clustering of galaxies in redshift space.

To explain how the distribution of galaxies is modified, let us consider a spherical overdensity region. It is initially filled with galaxies along concentric circles (represented respectively by dots and lines in figure 2.1).

This overdensity collapses towards its centre with galaxies on the same shell collapsing

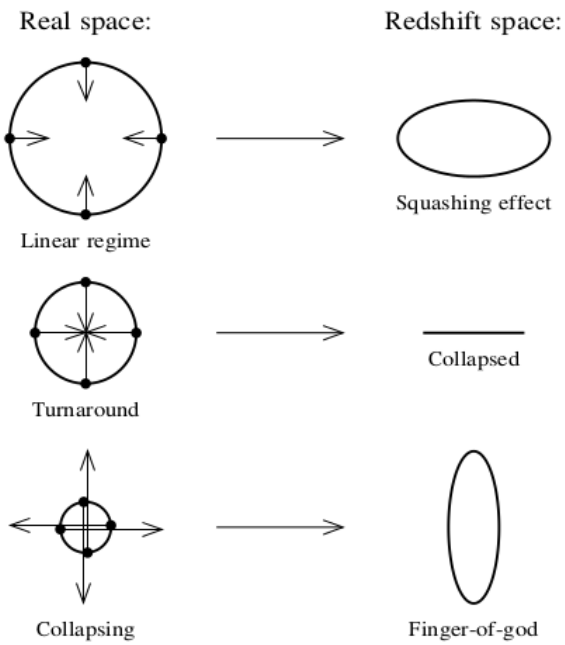

Figure 2.2: Detail of how peculiar velocities lead to the redshift distortions illustrated in Figure (2.1) [30].

with the same infall velocity. For an observer, galaxies with peculiar velocities perpendicular to the line of sight do not change their redshift, which is then given just by the normal expansion. On the contrary, galaxies with peculiar velocities along the line of sight will appear displaced.

Figure 2.2 shows in detail how the pattern in figure 2.1 is created. On large scales, when peculiar velocities are small, collapsing shells appear squashed along the line of sight. The squashing increases towards smaller scales since peculiar velocities tend to be bigger. At the turnaround point the peculiar velocities exactly equal the general Hubble expansion, so that the near and far parts of the shell appear collapsed to a single velocity in redshift space. At smaller scales, shells that have turned around and are collapsing appear turned "inside out" in redshift space, giving rise to an effect called *Fingers of God*.

Of course this distortion effect cannot be seen simply by eye in the distribution of galaxies, indeed recovering it it is a matter of statistic through the measure of the correlation function or the power spectrum. It is then necessary to construct a model for these two statistics that allows us to quantify this effect.

2.2 Modelling the RSD feature

Recall now the perturbed equations (1.27) and (1.28). In comoving coordinates and in the case of a collisionless fluid, the Newtonian approximation of this equation can be rewritten as:

$$\delta'_m + \theta_m = 0 \tag{2.5}$$

$$\theta'_m + \mathcal{H}\theta_m = -k^2\Phi\,, \tag{2.6}$$

where $\mathcal{H}$ is the Hubble parameter expressed in comoving coordinates and the prime represents the derivative with respect to the conformal time τ defined by $d\tau \equiv H_0 a_0 dt/a$. Φ is the gravitational potential that satisfies the Poisson equation. Combining these equations we can obtain the second order linear differential equation for the overdensity δ_m, that leads to growing and decaying solutions $\delta_m(\mathbf{r},\tau) \propto D(\tau)$, which evolve in time without change of shape. The interesting solution is the unstable growing solution. The linearized continuity equation (2.5) can then be written as:

$$\frac{Haf}{H_0 a_0}\delta_m + \theta = 0\,, \tag{2.7}$$

where f is the linear growth rate that we described in the first chapter (equation 1.39).

The linearized continuity equation (2.5) for the matter, evaluated at the present time, together with the linear bias model (1.50), yield the linearized continuity equation for galaxies

$$\beta\delta + \theta = 0\,, \tag{2.8}$$

where the dimensionless quantity β is the *distortion parameter* and it is related to the present day value f_0 of the linear growth rate and the bias factor b by

$$\beta = \frac{f_0}{b}\,. \tag{2.9}$$

In the linear regime, the overdensity δ^S in redshift space is related to the overdensity δ in real space by a *linear redshift distortion operators* S:

$$\delta^S = \mathbf{S}\delta\,, \tag{2.10}$$

where the superscript S identifies the quantities in redshift space. The starting point in the derivation of this operator is the conservation equation for galaxies, which expresses the fact

that the peculiar velocities displace along the line of sight, but they do not make galaxies appear or disappear

$$n^s(\mathbf{s})d^3s = n(\mathbf{r})d^3r. \tag{2.11}$$

If we define the overdensity in redshift space as $\delta^s(\mathbf{s}) \equiv (n^s(\mathbf{s}) - \bar{n}(\mathbf{s}))/\bar{n}(\mathbf{s})$, this equation can be rewritten as

$$\bar{n}(\mathbf{s})[1+\delta^s(\mathbf{s})]s^2ds = \bar{n}(\mathbf{r})[1+\delta(\mathbf{r})]r^2dr\,. \tag{2.12}$$

With the relation between redshift position and real position (equation (2.4)), this equation rearranges to

$$1+\delta^s(\mathbf{s}) = \frac{r^2\bar{n}(\mathbf{r})}{(r+v)^2\bar{n}(\mathbf{r}+v\hat{\mathbf{r}})}\left(1+\frac{\partial v}{\partial r}\right)^{-1}[1+\delta(\mathbf{r})]\,. \tag{2.13}$$

The next step is to linearize this equation. We can assume $|\delta(\mathbf{r})| \ll 1$, which also implies $|\partial v/\partial r| \ll 1$ and that peculiar velocities of galaxies are small compared to their distances from the observer, $|v| \ll r$. With these approximations and recalling that $\theta = \nabla \cdot v$, which implies (thanks to the continuity equation (2.8)) that $v = -\beta\frac{\partial}{\partial r}\nabla^{-2}\delta$, we can obtain the distortion equation $\delta^S = \mathbf{S}\delta$ with the distortion operator given by:

$$\mathbf{S} = 1+\beta\left(\frac{\partial^2}{\partial r^2}+\frac{\alpha(\mathbf{r})\partial}{r\partial r}\right)\nabla^{-2}\,, \tag{2.14}$$

where $\alpha(\mathbf{r})$ is the logarithmic derivative of r^2 times the real space selection function $\bar{n}(\mathbf{r})$.

In the plane-parallel, or distant observer, limit, the linear distortion operator (2.14) reduces to

$$\mathbf{S}^p = 1+\beta\frac{\partial^2}{\partial z^2}\nabla^{-2}\,, \tag{2.15}$$

where z is the distance along the line of sight. In Fourier space $(\frac{\partial}{\partial z})^2\nabla^{-2} = k_z^2/k^2 = \mu_{\mathbf{k}}^2$, where $\mu_{\mathbf{k}}^2 \equiv \hat{\mathbf{z}}\cdot\hat{\mathbf{k}}$ is the cosine of the angle between the wavevector $\mathbf{k}$ and the line of sight $\mathbf{z}$. Thus in Fourier space the plane-parallel distortion operator reduces to a diagonal operator

$$\mathbf{S}^p = 1+\beta\mu_{\mathbf{k}}^2\,, \tag{2.16}$$

so that a Fourier mode $\delta^s(\mathbf{k})$ in redshift space is amplified with respect to the real space mode by a factor $1+\beta\mu_{\mathbf{k}}^2$ according to the relation

$$\delta^s(\mathbf{k}) = (1+\beta\mu_{\mathbf{k}}^2)\delta(\mathbf{k})\,. \tag{2.17}$$

It follows from this equation that, in the plane-parallel approximation, the redshift space power spectrum $P^s(\mathbf{k})$ is amplified by $(1+\beta\mu_{\mathbf{k}}^2)^2$ over its unredshifted counterpart $P(k)$ according to the equation

$$P^s(\mathbf{k}) = (1+\beta\mu_{\mathbf{k}}^2)^2 P(k)\,, \tag{2.18}$$

firstly pointed out by Kaiser [41].

This formula has been translated into real space by Hamilton [30]

$$\xi(\mathbf{s}) = \left(1+\beta\frac{\partial^2}{\partial z^2}\nabla^{-2}\right)^2 \xi(\mathbf{r})\,, \tag{2.19}$$

who argued that this equation can be conveniently solved in the linear regime as a sum of spherical harmonics:

$$\xi_S^*(r_p,\pi) = \xi_0(s)P_0(\mu) + \xi_2(s)P_2(\mu) + \xi_4(s)P_4(\mu)\,, \tag{2.20}$$

where we have decomposed the correlation function in the direction perpendicular and parallel to the line of sight, r_p and π respectively. The subscript S denotes the quantity in redshift-space. Here P_l are the Legendre polynomials and ξ_l are the multipoles of the correlation function, which can be expressed as

$$\xi_0(s) = \left(1+\frac{2}{3}\beta+\frac{1}{5}\beta^2\right)\xi(r) \tag{2.21}$$

$$\xi_2(s) = \left(\frac{4}{3}\beta+\frac{4}{7}\beta^2\right)[\xi(r)-\bar{\xi}(r)] \tag{2.22}$$

$$\xi_4(s) = \frac{8}{35}\beta^2\left[\xi(r)+\frac{5}{2}\bar{\xi}(r)-\frac{7}{2}\bar{\bar{\xi}}(r)\right]\,, \tag{2.23}$$

and the barred quantities are defined as

$$\bar{\xi}(r) = \frac{3}{r^3}\int_0^r \xi(r')r'^2 dr' \tag{2.24}$$

$$\bar{\bar{\xi}}(r) = \frac{5}{r^5}\int_0^r \xi(r')r'^4 dr'\,. \tag{2.25}$$

In order to take into account the non-linear motions on small scales due to peculiar velocities, which cause the Fingers of God effect, it is necessary to convolve the correlation function ξ_S^* with the distribution function $f(v)$ of random pairwise velocities along the line of sight:

$$\xi(r_p,\pi) = \int_{-\infty}^{+\infty} \xi_S^{(L)}\left[r_p, \pi - \frac{v(1+z)}{H(z)}\right] f(v)dv. \tag{2.26}$$

The distribution $f(v)$ can be represented by an exponential form

$$f(v) = \frac{1}{\sigma_{12}\sqrt{2}} \exp\left(-\frac{\sqrt{2}|v|}{\sigma_{12}}\right) , \tag{2.27}$$

or by a Gaussian form

$$f(v) = \frac{1}{\sigma_{12}\sqrt{\pi}} \exp\left(-\frac{v^2}{\sigma_{12}^2}\right) . \tag{2.28}$$

In both expressions σ_{12} is a quantity independent of pair separation and is generally interpreted as the dispersion in the pariwise random peculiar velocities.

This model for the two-point correlation function depends on few quantities: β, σ_{12}, a reference cosmology used to convert angles and redshifts into distances and the true correlation function in real space. $\xi(r)$ can be obtained from theory or estimated from the galaxy catalogue itself. For example, a theoretical expression can be obtained from the galaxy luminosity function in the framework of the Halo Occupation Distribution assuming a theoretical prescription for the halo correlation function, as done e.g. by Yang et al. [78]. It is also possible to obtain $\xi(r)$ by Fourier transforming the theoretical matter power spectrum, computed assuming a fiducial cosmology, and then multiplying it by a bias function as it is done, for example, by Chuang & Wang ([13], [14]). As an alternative, it is possible to estimate $\xi(r)$ through a deprojection procedure of the measured $\xi_S(r_p, \pi)$. At first the observed redshift-space correlation function is projected along π:

$$\Xi(r_p) = 2\int_0^{\pi_{max}} \xi_S(r_p, \pi')d\pi' , \tag{2.29}$$

and then $\xi(r)$ is obtained via an Abel integral:

$$\xi(r) = \frac{1}{\pi}\int_r^{\infty} \frac{d\Xi(r_p')/dr_p}{\sqrt{r_p'^2 - r^2}} dr_p' , \tag{2.30}$$

where $r = \sqrt{r_p^2 + \pi^2}$.

2.3 Measurements of β from linear redshift distortions

RSD give us the possibility to recover some important information about the dynamics of galaxies and the amount of matter in the universe. In this section we want to briefly review some recent works about RSD giving an idea on how theory and observations are linked to each other.

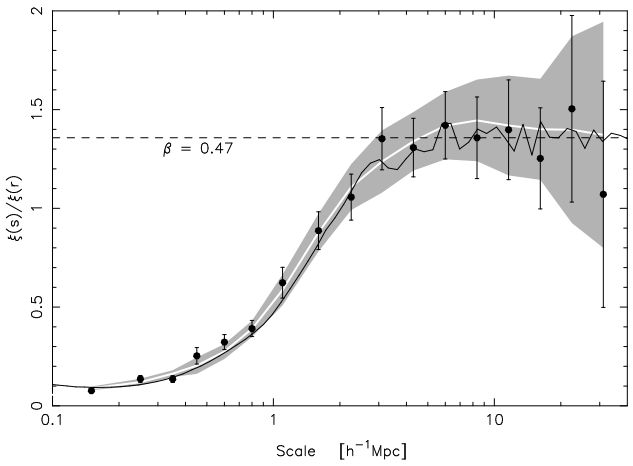

Figure 2.3: The ratio of $\xi(s)$ to $\xi(r)$ for the 2dFGRS from Hawkins et al. (2003) [33]

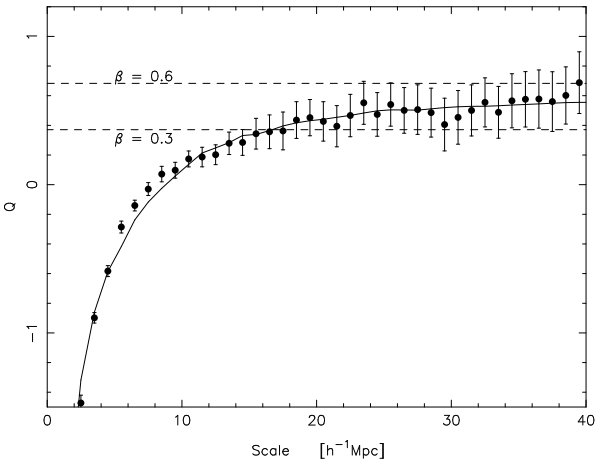

Figure 2.4: The Q factor (from equation (2.31)) for the 2dFGRS data from Hawkins et al. (2003) [33]. The solid lines represents a model with $\beta = 0.49$ and $\sigma_{12} = 506\ km\ s^{-1}$.

Hawkins et al. in 2003 [33] presented a detailed analysis of the 2-point correlation function $\xi(r_p, \pi)$ from the 2dF Galaxy Redshift Survey. The large size of the catalogue, of ≈ 220000 galaxies, allowed them to make accurate measurements of various properties of the galaxy clustering. They estimated $\xi(s)$ by averaging $\xi(r_p, \pi)$ at constant s, from which they measured the redshift-space clustering length $s_0 = 6.82 \pm 0.28\, h^{-1}\mathrm{Mpc}$ and slope $\gamma = 1.57 \pm 0.07\, h^{-1}\mathrm{Mpc}$, in the range $3 \leq s \leq 20\, h^{-1}\mathrm{Mpc}$. The projection of $\xi(r_p, \pi)$ along the π axis gives an estimate of the real-space correlation function $\xi(r)$, which can be fitted by a power-law with $r_0 = 5.05 \pm 0.25\, h^{-1}\mathrm{Mpc}$ and $\gamma = 1.67 \pm 0.03$, with the slope increasing at separation larger than $20\, h^{-1}\mathrm{Mpc}$. The authors gave a first estimate of

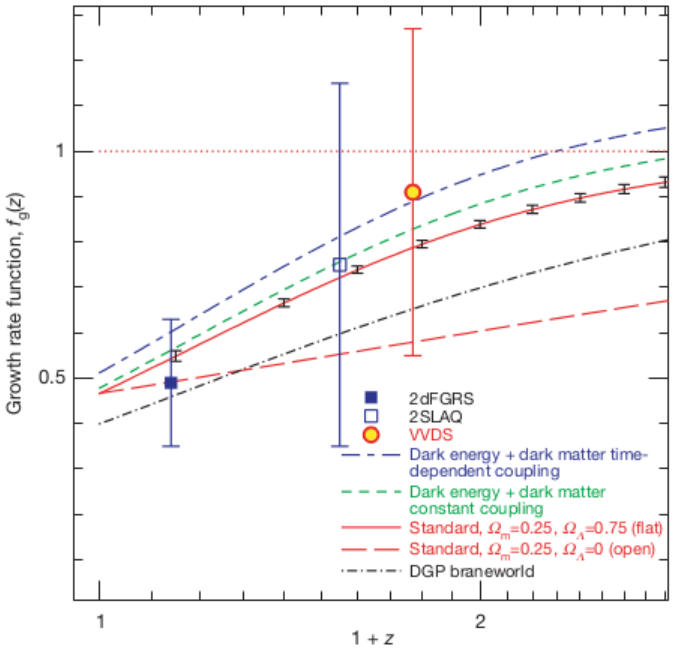

Figure 2.5: Measurements of the growth rate $f(z)$ from Guzzo et al. (2008) [29] compared to other works and theoretical predictions.

the distortion parameter through the ratio of real and redshift-space correlation functions on scale of $8 - 30\,h^{-1}\mathrm{Mpc}$ finding $\beta = 0.45 \pm 0.14$ (Figure 2.3). They also used the normalized quadrupole

$$Q(s) = \frac{\frac{4}{3}\beta + \frac{4}{7}\beta^2}{1 + \frac{2}{3}\beta + \frac{1}{5}\beta^2}\,, \tag{2.31}$$

since on large scales this quantity has an asymptotic behaviour which allowed to measure the distortion parameter. They found $\beta = 0.47^{+0.19}_{-0.16}$ (Figure 2.4). They also found an estimate of the distribution of random peculiar velocities comparing the projection of $\xi(r_p, \pi)$ along π and r_p. The result is that $f(v)$ is well approximated by an exponential with a velocity dispersion of $\sigma_{12} = 570 \pm 25\,\mathrm{km/s}$. Then they performed a maximum likelihood procedure to simultaneously fit the shape and the amplitude of $\xi(r)$ and the two redshift-space distortion effects parametrized by β and the velocity dispersion σ_{12}. They obtained $\beta = 0.49 \pm 0.09$ and $\sigma_{12} = 506 \pm 52\,\mathrm{km/s}$, finding also a strong correlation between these two values. Finally, using a constraint on bias from Verde et al. (2002) [75], they obtained $\beta(z = 0) = 0.47 \pm 0.08$ and $\Omega_m \approx 0.3$ for the present day matter density.

Guzzo et al. [29] measured the parameter β using the spectroscopic data from the

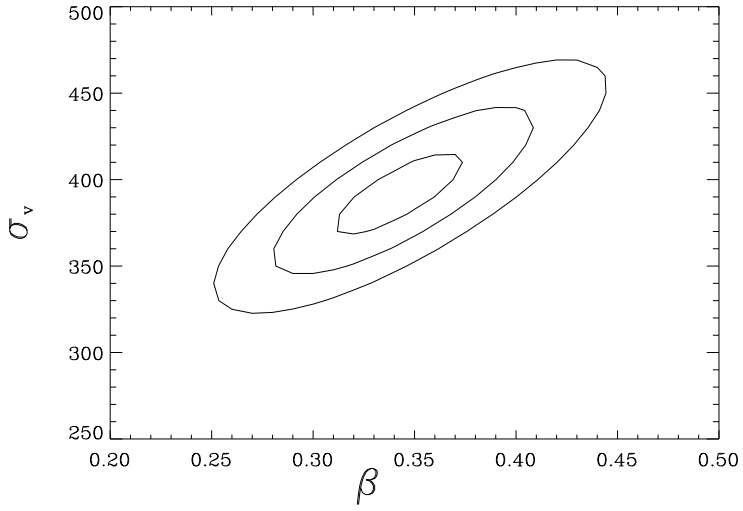

Figure 2.6: Contours for σ_{12} and β from Cabré & Gaztañaga (2009) [9] obtained using the quadrupole $Q(s)$ in the slice $z = 0.15 - 0.47$ at a distance between 5 and 60 $\mathrm{Mpc}\ h^{-1}$. Solid lines are 1, 2 and 3σ levels.

Wide part of the VIMOS-VLT Deep Survey. The redshift space correlation function was estimated from a subset of $5,895$ faint galaxies, covering an area of 4 square degrees. With a maximum likelihood procedure, they found $\beta = 0.70 \pm 0.26$ and $\sigma_{12} = 412\,\mathrm{km/s}$, where the error on β was obtained marginalizing over the pairwise velocity dispersion. To estimate the linear bias they used the relation $b_L = \sigma_8^{gal}(z = 0.77)/\sigma_8^{mass}(z = 0.77)$, where $\sigma_8^{gal}(z = 0.77)$ was measured directly from the sample by counting the number of galaxies in randomly placed spheres. The corresponding mass value was instead obtained by scaling the WMAP value to $z = 0.77$ using linear theory. In this way they found $b_L = 1.3 \pm 0.1$ correspoding to a growth rate of $f(z = 0.77) = \beta b_L = 0.91 \pm 0.36$ (Figure 2.5). They also proposed an empirical law which describes the dependency of the error of the β parameter on the mean density of objects n and on the volume V:

$$\frac{\delta\beta}{\beta} = \frac{50}{n^{0.44}V^{0.5}}\ . \tag{2.32}$$

Cabré & Gaztañaga in 2009 [9] studied the clustering of luminous red galaxies from the catalogue DR6 of the Sloan Digital Sky Survey (SDSS). In particular they wanted to obtain cosmological parameters exploiting redshift space distortions on large scale. They used the normalized quadrupole $Q(s)$ on large scale to calculate the distortion parameter $\beta =$

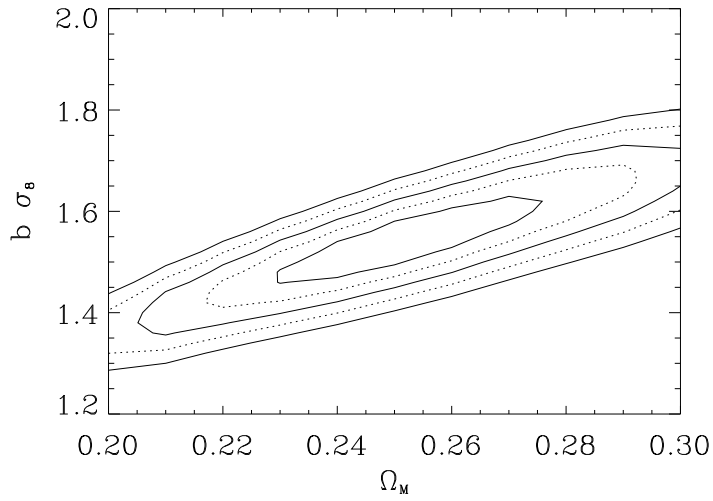

Figure 2.7: Contours for Ω_m and $b\sigma_8$ from Cabré & Gaztañaga (2009) [9] obtained using the full shape of the two-dimensional correlation function, for the slice $z = 0.15 - 0.34$. Solid lines are 1, 2 and 3σ levels (one degree of freedom) and dotted lines 1 and 2σ (two degrees of freedom).

0.34 ± 0.05 in the range $40 - 80\,\mathrm{Mpc}$. On small scales $Q(s)$ depends also on the pairwise velocity dispersion σ_{12}, so through a fit procedure in different slices of redshift the authors estimated both parameters finding best fit values for β in the range $[0.310 - 0.375]$ and for σ_{12} in the range $[365 - 415]\mathrm{km/s}$ (Figure 2.6). The great advantage of the normalized quadrupole introduced by Hamilton is that it does not depend on the overall amplitude or shape of the 2-point correlation function, that is, on cosmological parameters. They also checked that this value of β gives the correct ratio $\xi(s)/\xi(r)$ on large scale. From the shape of the redshift-space correlation function in the plane $r_p - \pi$ they obtained constraints on Ω_M and the amplitude $Amp = b(z)\sigma_8$, where $b(z)$ is the bias at redshift z and σ_8 is the mass variance. They found $\Omega_m = [0.225 - 265]$ and $b\sigma_8 = [1.47 - 1.65]$ (Figure 2.7). The high degeneracy between b and σ_8 can be broken thanks to redshift-space distortions through the parameter β, using the fact that $\beta = \Omega_m(z)^\gamma / b$. So it is possible to obtain σ_8 via the relation:

$$\sigma_8 = \frac{\beta\, Amp}{\Omega_m(z)^\gamma}\,. \tag{2.33}$$

The authors found $\sigma_8 = [0.79 - 0.91]$ and thereby $b = [1.73 - 1.94]$ for the bias and $f(\Omega_m) = [0.54 - 0.73]$ for the growth rate.

Their next step was to study the growth history in order to investigate any possible modification to the gravity theory through the parameter γ. They found consistence with standard gravity for $0.8 \leq \sigma_8 \leq 0.92$ at $1-\sigma$. DGP model is inconsistent with their results if $\sigma_8 < 0.84$.

Chuang & Wang in 2013 [14] presented measurements of $H(z)$, $D_A(z)$ and $\beta(z)$ at $z = 0.35$ using the multipoles of the correlation function measured from the SDSS DR7 LRGs in a MCMC likelihood analysis. The model they used incorporates the non-linear effects via the use of the "dewiggled" power spectrum including also the damping effect along the line of sight, to fully describe the BAO feature. They validated the method using 160 mock catalogues from the Las Damas simulations. They performed the likelihood analysis using at first the monopole ξ_0 and quadrupole ξ_2 and then adding the contribution of the hexadecapole ξ_4. These results are compared with the ones obtained using the full two-dimensional correlation function in their previous work [13], finding a good agreement between the two.

Contreras et al. [16] in 2013 studied the growth rate of cosmic structures to redshift $z = 0.9$ using more than $162,000$ galaxy redshifts from the WiggleZ Dark Energy Survey. They divided the data into four redshift slices with effective redshifts $z = [0.2, 0.4, 0.6, 0.76]$ and in each of the samples they measured the 2-point galaxy correlation function in parallel and transverse directions to the line of sight. Using a MCMC process the authors fitted a series of different models obtaining a convergence for the growth rate when excluding the small scale non-linear part of the data (transverse direction $r_p \leq 6\,h^{-1}\mathrm{Mpc}$, see Figure 2.8). They also tested the sensitivity of their results to the fiducial cosmological model adopted (Alcock-Paczynski effect [2]). They repeated the measurements assuming different fiducial values of Ω_m, finding a measured growth rate consistent with the predictions of standard gravity only in the range $0.2 < \Omega_m < 0.3$.

De la Torre et al. [22] analysed the first data release of the VIPERS survey, a catalogue of about $54,000$ galaxies at $0.5 < z < 1.2$, using the multipoles of the correlation function. Assuming a fixed shape of the mass power spectrum, consistent with the cosmological parameters obtained from WMAP9 [36], the authors performed a maximum likelihood analysis on the data to measure the growth rate at redshift $z = 0.8$. The measured value is

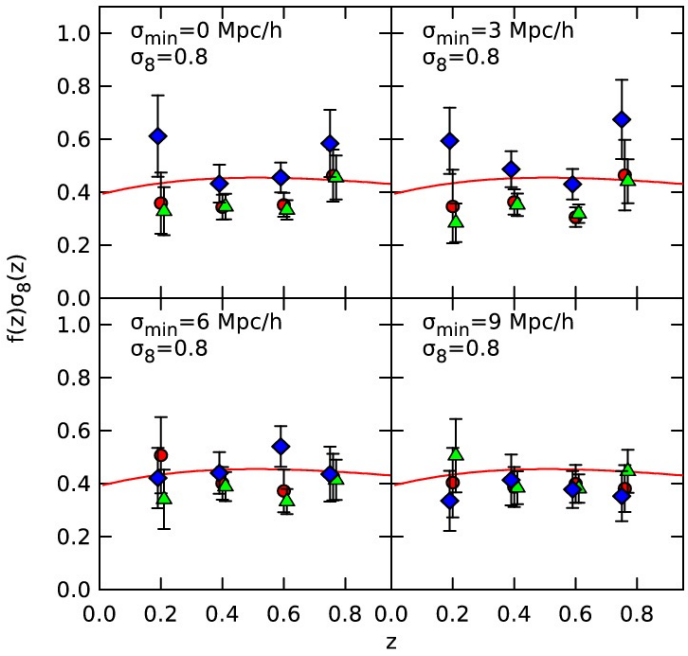

Figure 2.8: Fitted values for the growth rate from three different models obtained by [16] in four redshift slices for different data cuts $\sigma > \sigma_{min}$. The red line in each panel represents the prediction of a fiducial ΛCDM model with $\Omega_m = 0.27$ and $\sigma_8 = 0.8$.

$f(z)\sigma_8(z) = 0.47 \pm 0.08$ which is consistent with the General Relativity prediction in a flat ΛCDM universe with cosmological parameters given by WMAP9, for which the expected value is $f(z)\sigma_8(z) = 0.45$ (see Figure 2.9). The authors also found that their result is not significantly altered if they assume a Planck cosmology [57], showing that it is insensitive to the Alcock-Paczynski distortions of the correlation function.

Howlett et al. [37] measured RSD in the 2-point correlation function of a sample of $63,163$ spectroscopically identified galaxies with $z < 0.2$ from the SDSS DR7 Main Galaxy Sample (MGS). They modeled the monopole and the quadrupole of the correlation function and fitted to the MGS data measuring $f\sigma_8 = 0.53 \pm 0.19$ when using the full shape of the correlation function, whereas $f\sigma_8 = 0.44^{+0.16}_{-0.12}$ when assuming a fiducial cosmology based on the recent Planck results [57], showing that the Alcock-Paczynski effect contributes to the uncertainties of the growth rate and should not be neglected (see Figure 2.10). The method has been validated using 1000 mock catalogues which allow also to estimate the

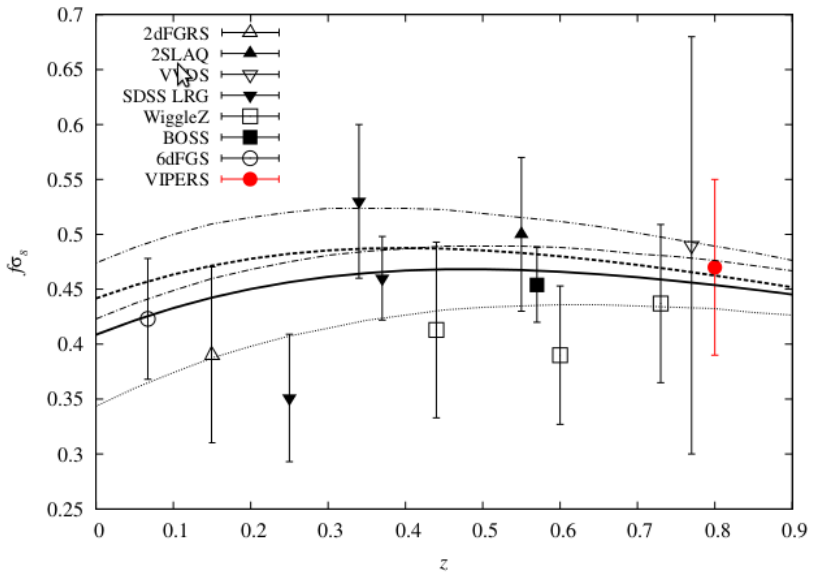

Figure 2.9: A plot of $f\sigma_8$ versus redshift from [22], showing the VIPERS result (red circle) compared to other measurements. The thick solid (dashed) curve corresponds to the prediction for General Relativity in a ΛCDM model with WMAP9 (Planck) parameters, while the dotted, dot-dashed, and dot-dot-dashed curves are respectively Dvali-Gabadaze-Porrati [21], coupled dark energy, and $f(R)$ model expectations.

covariance matrix for the correlation function. Given the measurements of the growth factor, the authors measured the growth index γ finding $\gamma = 0.58^{+0.50}_{-0.30}$ when including Planck data and $\gamma = 0.67^{+0.18}_{-0.15}$ when also including BOSS-DR11 CMASS measurements of the growth rate. They improved these constraints including the BAO from the full fit of the shape of the correlation function, finding $\gamma = 0.54^{+0.25}_{-0.24}$ and $\gamma = 0.64 \pm 0.09$ respectively. All of these results are consistent with the prediction of General Relativity $\gamma \simeq 0.55$ and the constraints from other measurements at different redshifts.

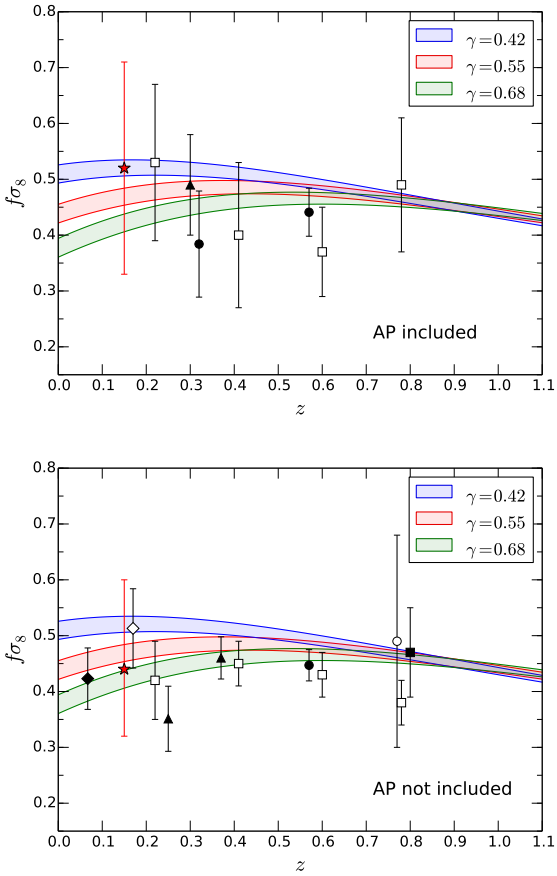

Figure 2.10: Comparison of measurements of the growth rate from [37] (red star) and a variety of galaxy surveys below $z = 0.8$ using the two-point clustering statistics. The results are split in two groups: those that perform a full shape fit and hence include the Alcock-Paczynski degeneracy and those that just fit the growth rate for a fixed cosmology, neglecting this degeneracy.

Chapter 3

From theory to practice

In order to perform a parameter estimation one needs a dataset, a model which describes the data, and a likelihood function, that is a function of the parameters that tells us how good is a model in describing the data. In our case the dataset is given by the correlation function of galaxies which is measured from a cosmological simulation. The model is the one described in the previous chapter, whose parameters are the cosmological parameters embedded in the theoretical correlation function, the redshift distortion parameter β and the pairwise velocity dispersion of galaxies σ_{12}. The likelihood is performed through a Markov Chain Monte Carlo (MCMC) analysis. In this chapter we will briefly describe all these technical aspects of our work.

3.1 How to measure correlation function

Studying the clustering properties of the universe is a matter of statistics and the two-point correlation function represents a powerful tool in this sense. It can be interpreted as the function that tells us how galaxies distribute around each other, describing the probability of finding a galaxy in a certain position in space given the presence of another galaxy at a comoving distance r from it.

Let us consider N objects in a volume V and focus our attention on a small volume dV chosen randomly inside V. Then $dN = \rho_0 dV$ is the average number of objects in the infinitesimal volume, with $\rho_0 = N/V$ the mean density in the entire volume V. The quantity dN represents also the probability to find an object in the volume dV. In the same way we can define the number of pairs made up by the objects of for two infinitesimal volumes dV_a and dV_b at a distance r_{ab}, $dN_{ab} = \langle n_a n_b \rangle = \rho_0^2 dV_a dV_b$, which represents the

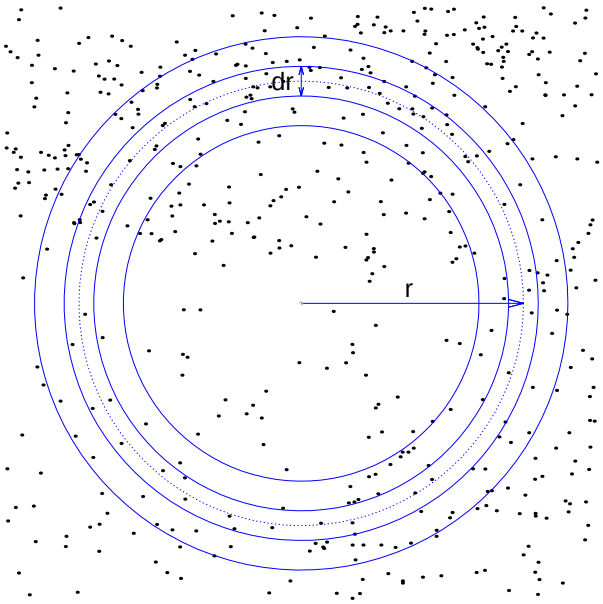

Figure 3.1: An example of shell structure to measure the correlation function. The shells, drawn for simplicity in 2 dimension, are centered on a given object. One has to count the number of objects in each shell and repeat again the procedure centering the shell structure on each object. The correlation function at a given radius is obtained averaging the values obtained and comparing them with the corresponding values for a uniform distribution.

probability to find an object in dV_b given an object in dV_a. This relation holds in the case of a uniform random distribution. In presence of a clustered distribution we can rewrite it as

$$dN_{ab} = \langle n_a n_b \rangle = \rho_0^2 dV_a dV_b [1 + \xi(r_{ab})] \,, \tag{3.1}$$

where $\xi(r_{ab})$ describes the excess or defect of probability, with respect to a uniform distribution, of finding an object at a distance r_{ab} from another one.

Equation (3.1) follows from the definition of density constrast (equation (1.42)) written as a function of the number of objects $\delta(x_a) = dN_a/\rho_0 dV_a - 1$, which leads to:

$$\langle \delta(x_a)\delta(x_b) \rangle = \frac{dN_{ab}}{\rho_0^2 dV_a dV_b} - 1 = \xi(r_{ab}) \,. \tag{3.2}$$

Given a distribution of objects, the most direct method to estimate the correlation function is to count how many objects fall inside a shell of radius r centered on a given object (see Figure 3.1). Then the value of the correlation function is obtained by comparing the mean value of objects per shell and the expected value for a uniform distribution.

However for a practical point of view, this is not the best method, since a survey has often irregular contours. The shell centered in galaxies nearby the edges will be partially empty and the correlation function will be underestimated. To avoid this problem the approach adopted is the following: a random catalogue is constructed with the same geometry and the same selection function of the real catalogue; the value of the correlation function is then estimated by comparing the number of pairs of real galaxies at a given distance and the pairs of random galaxies. So given a generic galaxy centered in a volume dV, $n(r) = (N_D/V)[1 + \xi(r)]dV$ is the number of real galaxies that we expect to find in that volume, with N_D the total number of galaxies in the volume V. Then, inverting the relation we obtain

$$1 + \xi(r) = \frac{V}{N_D^2} \sum_{i=1}^{N_D} \frac{n_i(r)}{dV_i} = \frac{V}{N_D^2} \frac{2n_D(r)}{\langle dV \rangle} \,, \tag{3.3}$$

where $n_D(r)$ is mean value of $n_i(r)$ over all the particles. The same relation holds for the random particles, so we have:

$$\langle dV \rangle = \frac{2n_R(r)V}{N_R^2} \,, \tag{3.4}$$

since in this case $\xi(r) = 0$. Then combining these two relations we obtain the *natural estimator*

$$\hat{\xi}_N(r) = \frac{DD(r)}{RR(r)} - 1 \,, \tag{3.5}$$

where $DD(r) = n_D/N_D^2$ and $DD(r) = n_R/N_R^2$. This estimator clearly goes to zero when the number of pairs in the real catalogue is equal to the number of pairs in the random catalogue. This is the most natural way to estimate the correlation function.

Other estimators has been proposed throughout the years, considering also pairs made by a random and a real object, in order to minimize the variance:

- Davis and Peebles [19]:

$$\hat{\xi}_{DP}(r) = \frac{DD(r)}{DR(r)} - 1 \,, \tag{3.6}$$

- Hewett [34]:

$$\hat{\xi}_{He}(r) = \frac{DD(r)_D R(r)}{RR(r)} \,, \tag{3.7}$$

- Hamilton [31]:

$$\hat{\xi}_{Ha}(r) = \frac{DD(r)RR(r)}{DR^2(r)} - 1 \,, \tag{3.8}$$

- Landy-Szalay [45]:

$$\xi_{LS}(r) = \frac{DD(r) - 2DR(r) + RR(r)}{RR(r)} \,. \tag{3.9}$$

Generally, the estimation of the correlation function for current galaxy surveys makes use of the *Landy-Szalay* estimator since it has been shown that it is characterized by minimal variance and is stable with respect to variations in density of the random catalogue ([58, 42]). Indeed this is the estimator that we use in our analysis.

3.2 The BASICC simulation

One of the building blocks of our work is the BASICC simulation, the Barionic Acoustic oscillation Simulation at the Institute for Computational Cosmology, by Angulo et al. [4]. One of the advantages of using numerical simulations is that we know a priori the value of the parameters we want to measure. Moreover simulations solve the problem of having only one universe available for observations. Indeed it is possible to construct many simulations, with the same cosmological parameters, and repeat the measurement for each of them. In particular, comparing the theoretical values of the parameters we want to measure with the mean measured estimates, we can assess the systematic errors due to the method, while the scatter between measurements can give us an idea of the expected statistical errors.

The BASICC simulation has been explicitly designed to study Baryon Acoustic Oscillations (BAO) features in the clustering pattern, so its volume is large enough to follow the growth of fluctuations in a wide range of scales up to those of BAO. At the same time the resolution is high enough that it is possible to split the whole box in sub-cubes whose volumes match that of the typical ongoing surveys, still preserving a good statistic on scales which are central in our analysis. This simulation is made up by 1448^3 dark matter particles of mass $M_{part} = 5.49 \times 10^{10}\, h^{-1}\, M_\odot$, in a periodic box of side $1340\, h^{-1}$Mpc. The cosmological model adopted is a ΛCDM model with $\Omega_M = 0.25$, $\Omega_\Lambda = 0.75$, $\sigma_8 = 0.9$ and $h = H_0/(100\,\mathrm{km\,s^{-1}\,Mpc^{-1}}) = 0.73$. Dark matter haloes are identified using a Friends-of-Friends (FOF) algorithm [18] with a linking length of 0.2 times the mean particle separation. This means that a group of particles can be considered a halo if for each particle another one can be found at a distance smaller than the linking length. The minimum number of particles per halo is $N_{part} = 20$, so that the minimum mass halo is $M_{halo} = 20 \cdot \mathrm{M_{part}} \simeq 1.10 \times 10^{12}\, h^{-1}\, M_\odot$.

Since we want to exploit RSD features, we need to simulate this effect artificially. This means that we need to "observe" the simulation assuming that the only information about the distances of the objects comes from their redshift, as it happens in real surveys. For this purpose let us consider a snapshot of the simulation at a given redshift z and place its center at the corresponding comoving distance

$$r_c(z) = c\int_0^z \frac{dz'}{H(z)} = \int_0^z \frac{c}{H_0\sqrt{\Omega_M + \Omega_\Lambda(1+z')^3}}dz' \,, \tag{3.10}$$

where the last equality holds for a flat cosmology. In other words we transform the positions (X_i, Y_i, Z_i) of each object in a cube of side L into new comoving coordinates

$$-\frac{L}{2} \leq X \leq \frac{L}{2} \,, \quad r_c - \frac{L}{2} \leq Y \leq r_c + \frac{L}{2} \,, \quad -\frac{L}{2} \leq Z \leq \frac{L}{2} \,, \tag{3.11}$$

where we arbitrarily chose the direction of the Y axis for the translation. In this way each object is assigned with a comoving distance $r_{c,i} = \sqrt{X_i^2 + Y_i^2 + Z_i^2}$ and hence with a real undistorted redshift z_i obtained inverting equation (3.10). We then add the Doppler contribution to obtain the observed distorted redshift, as

$$\hat{z}_i = z_i + \frac{v_r}{c}(1 + z_i) \,, \tag{3.12}$$

where v_r is the line of sight peculiar velocity. With this procedure we obtain a mock catalogue from which it is possible to compute the redshift space position of the objects through equation (3.10), using $\hat{z}_i$ instead of z_i, which is exactly what we were searching for.

3.3 Markov Chain Monte Carlo technique

Our analysis is performed using the Markov Chain Monte Carlo (MCMC) technique, which is largely diffuse in cosmology. Here we want to give a brief review of this technique since it is another fundamental building block of our work.

Let us suppose that we want to measure some set of cosmological parameters $\mathbf{a}_{true}$. Of course the real parameter values are unknown. When we observe the universe we are actually observing a statistical realization, $\mathbf{a}_0$, of this parameter set. If we could have infinite other realizations we could measure different sets of parameters $\mathbf{a}_i$ for each hypotetical dataset D_i, and this would lead to the knowledge of the distribution $\mathbf{a}_{true} - \mathbf{a}_i$, which is what we would need to know to estimate uncertainties in our measurement $\mathbf{a}_0$. The usual procedure is then to assume that $\mathbf{a}_0$ is not so far from $\mathbf{a}_{true}$ so that it would not be such a

big mistake to replace $\mathbf{a}_{true} - \mathbf{a}_i$ with $\mathbf{a}_0 - \mathbf{a}_i$. Then we can "simulate" many synthetic realizations of a universe where $\mathbf{a}_0$ is the true underlying model, that is compute different models of the universe varying all the parameters. In this way we could be able to estimate $\mathbf{a}_0 - \mathbf{a}_i$ and map our desired multi-dimensional probability distribution.

The problem here is that this procedure can be computationally very expensive when the parameter set is big. For example, for CMB studies the considered models considered have from 6 to more than 11 parameters, and a grid-based likelihood analysis would require a prohibitive amount of time. For this reason Christensen and Meyer [11] proposed to use MCMC to investigate the likelihood space. In brief this approach has become the standard tool for CMB analysis and cosmology in general.

MCMC is a method to sample the *posterior distribution* $\mathcal{P}(\mathbf{a}|x)$ of the parameters, which is the probability of having $\mathbf{a}$ given the event x. This procedure exploits the Bayes' Theorem:

$$\mathcal{P}(\mathbf{a}|x) = \frac{\mathcal{P}(x|\mathbf{a})\mathcal{P}(\mathbf{a})}{\int \mathcal{P}(x|\mathbf{a})\mathcal{P}(\mathbf{a})d\mathbf{a}}\,, \tag{3.13}$$

where $\mathcal{P}(x|\mathbf{a})$ is the *likelihood* and $\mathcal{P}(\mathbf{a})$ is the *prior*. The likelihood is the probability of the data given the model and in many cases can be approximated by a Gaussian. The prior expresses our knowledge about parameters. This may be the results of previous experiments or may be a theoretical prior in absence of any data. In such cases, it is common to assume that all values of the parameters are equally likely and take $\mathcal{P}(\mathbf{a}) = \text{const}$. This is referred to as flat prior.

The MCMC generates random draws from the posterior distribution that are fair samples of the likelihood, essentially doing a random walk in the parameter space such that the probability of being at any position in this space is proportional to the posterior probability.

Here it is a list of the necessary steps to run a MCMC:

1. start with a set of cosmological parameters $\mathbf{a}_1$ and compute your model and your likelihood, $\mathcal{L}_1$;

2. take a random step in parameter space to obtain a new set of cosmological parameters $\mathbf{a}_2$;

3. compute your model for the new set of parameters and the new likelihood $\mathcal{L}_2$;

4. if the ratio $\mathcal{L}_2/\mathcal{L}_1 \geq 1$ take the new step: save the parameter set $\mathbf{a}_2$ in a chain and go back to step 2 generating a new parameter set.

If $\mathcal{L}_2/\mathcal{L}_1 < 1$ draw a random number x from a uniform distribution from 0 to 1. If $x \geq \mathcal{L}_2/\mathcal{L}_1$ don't take the step: reject the parameter set $\mathbf{a}_2$, save again the parameter set $\mathbf{a}_1$ and go back to step 2 generating a new parameter set; If $\mathcal{L}_2/\mathcal{L}_1 \geq 1$ take the step and go back to step 2;

5. Repeat the procedure until a convergence criterion is satisfied and the chains have enough points to provide a resonable sampling of the posterior distribution.

Two key points in the implementation of MCMC are the *convergence* of the chains and the *mixing*, which is strictly related to the steps used to span the parameter space.

After an initial period called *burn-in*, all the further samples in the chain can be thought of as coming from a stationary distribution, that is the chain has no dependence on the starting location. After the stationarity has been reached we need to determine when the chain has converged. One of the most used methods is the one proposed by Gelman and Rubin [27]. This method compares several chains drawn from different starting point (the initial parameter set is different for each chain) checking when they are indistinguishable. The chains are monitored by recording the quantity

$$\hat{R} = \frac{\frac{N-1}{N}W + \frac{B}{N}\left(1 + \frac{1}{M}\right)}{W}\,, \tag{3.14}$$

where M is the number of chains and N is half the number of the chains element. W represents the variance within a chain and B is the variance between chains. Then the quantity $\hat{R}$ is the ratio of two estimates of the variance in the target distribution, and it is recorded for each parameter. When the convergence is achieved, as N becomes bigger and bigger, this ratio should approach to unity. How much this value should be close to unity is still a matter of debate. It is usual to stop the chains when $\hat{R} < 1.1$ for all parameters. However one should check that this value does not increase once it has reached a value close to unity, otherwise the convergence can be prematurely declared [28].

Another fundamental problem is to check if there are areas of the target distribution that are not been covered by a chain. If the MCMC could run for a very long time the chain would cover the whole distribution, but in the short term it cannot happen. It is thus crucial that the chain achieves a good mixing, that means that the chain needs to move rapidly throughout the parameter space. A good mixing can be obtained with a step size optimization. The choice of the step size in the Markov Chain is crucial to improve the chain

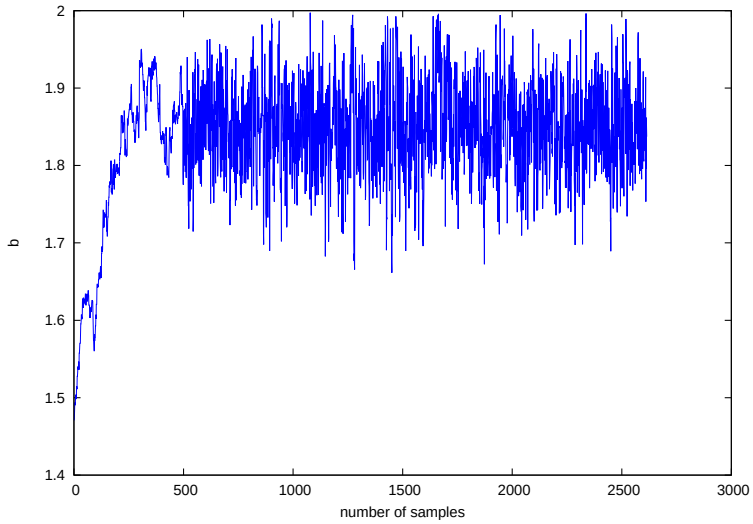

Figure 3.2: An example of well mixed and converged chain: after the burn-in period the chain reaches stationarity: each position in space depends only from the previous one and not from the starting point

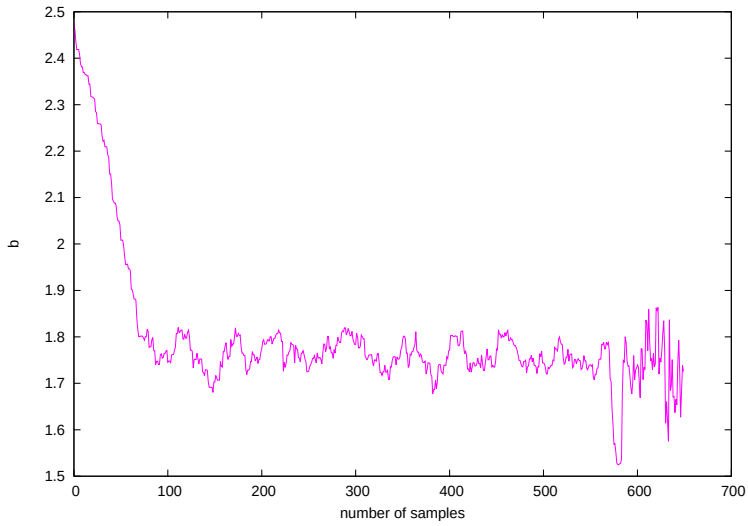

Figure 3.3: An example of bad mixed and unconverged chain: after the burn-in phase the chain does not reach the stationarity and does not converge.

efficiency and speed up the convergence. If the step size is too big, the acceptance rate will be very small, but the mixing will be good; if the step size is too small, the acceptance rate will be high but the chain will exhibit poor mixing. In both cases the convergence will require a conspicuous amount of time. Examples of good mixed and bad mixed chains are shown in Figures 3.2 and 3.3 respectively. Figure 3.2 shows a chain that makes its way to the targeting distribution. This chain can be used for parameter estimation after having discarded the burn-in period of 500 chain steps. Figure 3.3 instead shows a chain that offers no evidence of convergence and is entirely unsuitable for making parameter estimation. Using chains that have not fully explored the likelihood surface for determining cosmological parameters will yield wrong results.

Once the chains have converged we can quote the best fit values and errors for each parameter. However, of all the model parameters a_i, some of them may be uninteresting, but also it may be that we are interested on constraining only one parameter at a time, rather than to jointly constrain two or more parameters simultaneously. One then *marginalises* over the uninteresting parameters, by integrating the posterior distribution:

$$\mathcal{P}(a_1|D) = \int da_2 ... da_n \mathcal{P}(\mathbf{a}|x) \; . \tag{3.15}$$

Often one sees marginal distribution of all parameters in pairs, as a way to present some complex results. In this case two variables are left out of the integrations.

Chapter 4

Parameters estimation and the covariance matrix issue

In this chapter we are going to explain in detail the method we use to estimate the cosmological parameters, focusing on how the likelihood analysis has been performed and illustrating the issues related to the covariance matrix. We also show the preliminary tests that helped us to assess the validity of the method.

4.1 Measuring the correlation function

We focus our attention on the output of the BASICC simulation at $z = 1$, which is a central value in the range of redshifts that will be explored in future redshift surveys, like Euclid.

We split the whole box simulation in N^3 sub-boxes, with $N = 3$, obtaining 27 sub-boxes. This is a good compromise between having a good statistic and having a large sample volume of $\approx 447^3\ \mathrm{Mpc}^3\ h^{-3}$. The correlation function is measured from the mock catalogues extracted from these sub-cubes, using the Landy & Szalay estimator [45]:

$$\xi_{LS}(r_p, \pi) = \frac{HH(r_p, \pi) - 2HR(r_p, \pi) + RR(r_p, \pi)}{RR(r_p, \pi)}\,, \tag{4.1}$$

where r_p and π are respectively the separation perpendicular and parallel to the line of sight (LOS), which is defined as the direction from the observer to the center of the pair. HH, RH and RR represent the normalized halo-halo, halo-random and random-random pair counts in a certain distance range respectively. The random catalogues have $N_R = 50$ times the number of objects of the mock catalogues. We chose to fix $N_R = 50$ in order to reduce the shot noise that affects in particular less dense catalogues, as it can be seen in Figure 4.1, which shows that increasing the number of objects in the random catalogue gives a better

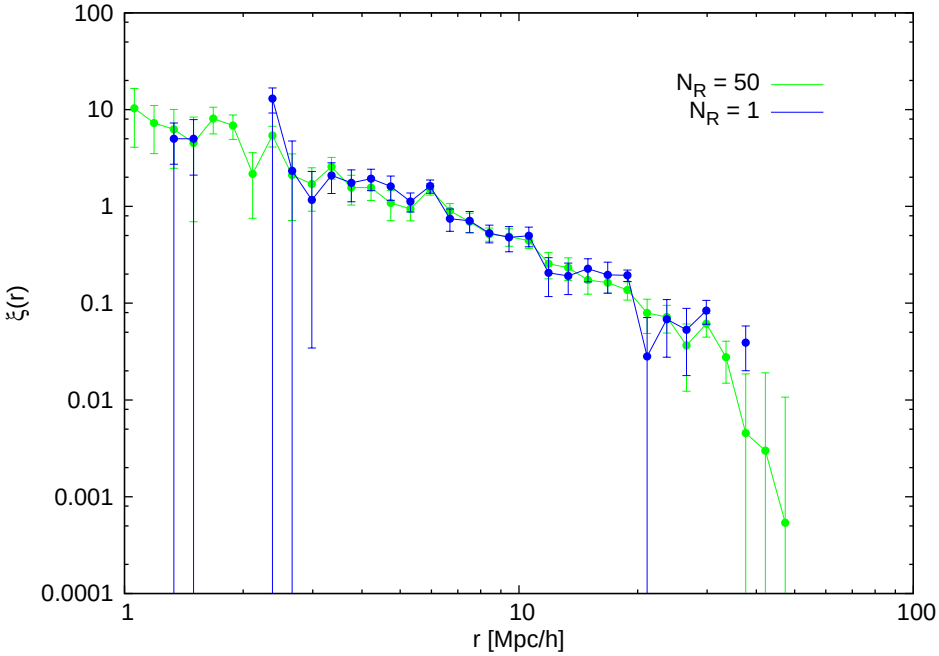

Figure 4.1: Correlation function in redshift space for the less dense catalogue having a mass threshold $M_{cut} = 1.1.0 \times 10^{12}\ h^{-1}\ M_{\odot}$. In blue the correlation function is measured using a random catalogue with as many objects as the mock catalogue, whereas in green we show the one measured using 50 times the number of objects of the mock catalogue. The error bars represent the square root of the diagonal elements of the covariance matrix.

estimate of the correlation function, allowing us to reach a good signal on all scales.

In Figure 4.2 we show the two-dimensional correlation function from the 27 mocks for the catalogue of haloes with minimum mass equal to $M_{cut} = 1.10 \times 10^{12} M_{\odot}$, which is the catalogue that we are going to use in the tests illustrated in this chapter. The squashing effect along the line of sight due to the RSD is clearly visible, whereas the Fingers of God, the elongation on small scales caused by non-linear motions, are almost absent due to the lack of substructures in the DM FOF haloes. The bin used to compute the two-dimensional correlation function is $1\,\mathrm{Mpc}\,h^{-1} \times 1\,\mathrm{Mpc}\,h^{-1}$, and the maximum radius at which we evaluate it is $s = \sqrt{r_p^2 + \pi^2} = 50\,\mathrm{Mpc}\,h^{-1}$.

Once we have measured the correlation function in two dimensions using eq. (4.1) we compute the multipoles of the correlation function, defined as follows:

$$\begin{aligned} \xi_l &= \frac{2l+1}{2} \int_{-1}^{1} \xi(r_p, \pi) P_l(\mu) d\mu \\ &= \frac{2l+1}{2} \int_{0}^{\pi} \sqrt{1-\mu^2}\, \xi(r_p, \pi) P_l(\mu) d\theta \ , \end{aligned} \tag{4.2}$$

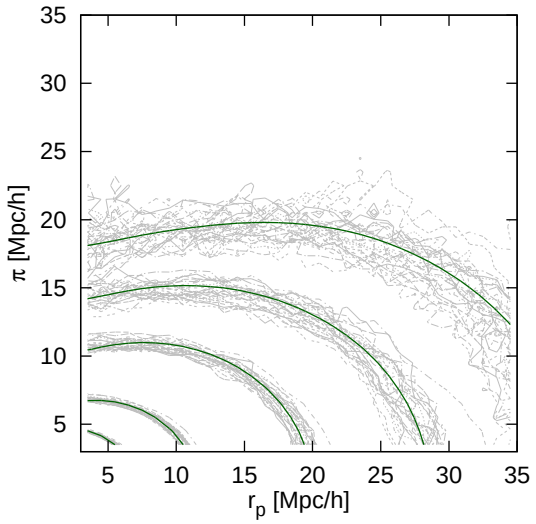

Figure 4.2: Correlation function in two dimensions. The grey lines represent the correlation function measured from the 27 mock catalogues. The green lines represent the mean best fit model. The isocorrelation contours are set arbitrarily to $\{0.05, 0.1, 0.2, 0.5, 1\}$.

where $P_l(\mu)$ are the Legendre polynomials and μ is the cosine of the angle between the separation vector and the line of sight: $\mu \equiv \cos\theta = \pi/r_p$. The first four multipoles are shown in Figure 4.3.

4.2 Modelling the correlation function

In order to model the correlation function we need at first to compute the non-linear power spectrum $P_{nl}(k)$ at $z = 1$ using CAMB [48] plus the HALOFIT [70] correction that accounts for non-linearities. The theoretical DM real space correlation function $\xi_{DM}(r)$ is then obtained by Fourier transforming the non-linear power spectrum, according to equation (1.48) from Chapter 1. To obtain the halo correlation function we multiply it by a bias factor: $\xi_{halo} = b^2\xi_{DM}$. The two-dimensional correlation function in redshift space is now

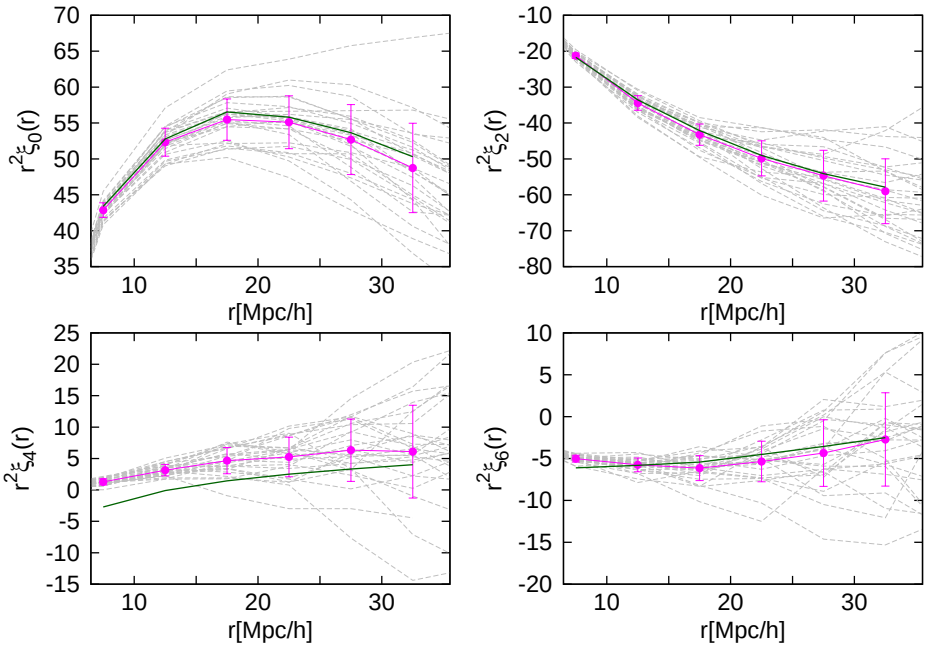

Figure 4.3: Multipoles of the correlation function: monopole ξ_0 (top left panel), quadrupole ξ_2 (top right panel), hexadecapole ξ_4 (bottom left panel), hexacontatetrapole ξ_6 (bottom right panel). The grey lines represent the correlation function measured from the 27 mocks. The magenta lines represent the mean multipoles over the 27 mocks, the error bars being the square root of the diagonal elements of the covariance matrix. The best fit mean model is represented by the green lines.

computed using the model described in Chapter 2. We compute at first the multipoles:

$$\xi_0(s) = \left(1+\frac{2}{3}\beta+\frac{1}{5}\beta^2\right)\xi_{halo}(r) \tag{4.3}$$

$$\xi_2(s) = \left(\frac{4}{3}\beta+\frac{4}{7}\beta^2\right)[\xi_{halo}(r)-\bar{\xi}_{halo}(r)] \tag{4.4}$$

$$\xi_4(s) = \frac{8}{35}\beta^2\left[\xi(r)+\frac{5}{2}\bar{\xi}_{halo}(r)-\frac{7}{2}\bar{\bar{\xi}}_{halo}(r)\right], \tag{4.5}$$

where the barred quantities are defined as

$$\bar{\xi}_{halo}(r) \equiv \frac{3}{r^3}\int_0^r \xi_{halo}(r')r'^2dr' \tag{4.6}$$

$$\bar{\bar{\xi}}_{halo}(r) \equiv \frac{5}{r^5}\int_0^r \xi_{halo}(r')r'^4dr'\,. \tag{4.7}$$

Then, we obtain the two-dimensional correlation function via the formula:

$$\xi_S^*(r_p,\pi) = \xi_0(s)P_0(\mu)+\xi_2(s)P_2(\mu)+\xi_4(s)P_4(\mu)\,. \tag{4.8}$$

In order to take into account the non-linear motions on small scales due to peculiar velocities, we convolve the correlation function ξ_S^* with the distribution function $f(v)$ of random pairwise velocities along the line of sight:

$$\xi(r_p, \pi) = \int_{-\infty}^{+\infty} \xi_S^* \left[r_p, \pi - \frac{v(1+z)}{H(z)} \right] f(v) dv \,, \tag{4.9}$$

where $f(v)$ can be represented by an exponential form

$$f(v) = \frac{1}{\sigma_{12}\sqrt{2}} \exp\left(-\frac{\sqrt{2}|v|}{\sigma_{12}} \right) . \tag{4.10}$$

The non linear model of eq. (4.9) can be now integrated to obtain the multipoles models according to equation (4.2).

4.3 Likelihood analysis and covariance matrix

We use the 27 mock catalogues extracted from the BASICC simulation to estimate the covariance matrix, which is constructed as follows:

$$C_{ij} = \frac{1}{N-1} \sum_{k=1}^{N} (\bar{X}_i - X_i^k)(\bar{X}_j - X_j^k) \,, \tag{4.11}$$

where the sum is over the number of mocks N and $\mathbf{X}$ is the data vector containing the measured correlation function; $\bar{X}_i$ is the mean value over the N mocks of the i^{th} element of the data vector, while X_i^k is the value of the i^{th} component of the vector corresponding to the k^{th} mock catalogue. The likelihood is taken to be proportional to $\exp(-\chi^2/2)$ [59], where χ^2 is defined as:

$$\chi^2 = \sum_{i,j=1}^{N_{bins}} (X_{th,i} - X_{obs,i}) C_{ij}^{-1} (X_{th,j} - X_{obs,j}) \,, \tag{4.12}$$

where N_{bins} is the length of the vector X, X_{th} is the theoretical vector and X_{obs} is the data vector.

When using the multipoles in the likelihood analysis the data vector is made up by the components of the multipoles vectors as follows:

$$\mathbf{X} = \{\xi_0^{(1)}, \xi_0^{(2)}, ..., \xi_0^{(M)}, \xi_2^{(1)}, \xi_2^{(2)}, ..., \xi_2^{(M)}, \xi_4^{(1)}, ..., \xi_4^{(M)}, \xi_6^{(1)}, ..., \xi_6^{(M)}, ...\} \,, \tag{4.13}$$

where M is the dimension of each vector. The covariance is now a sort of block matrix in which the contribution of the covariance between multipoles is present. In this thesis we

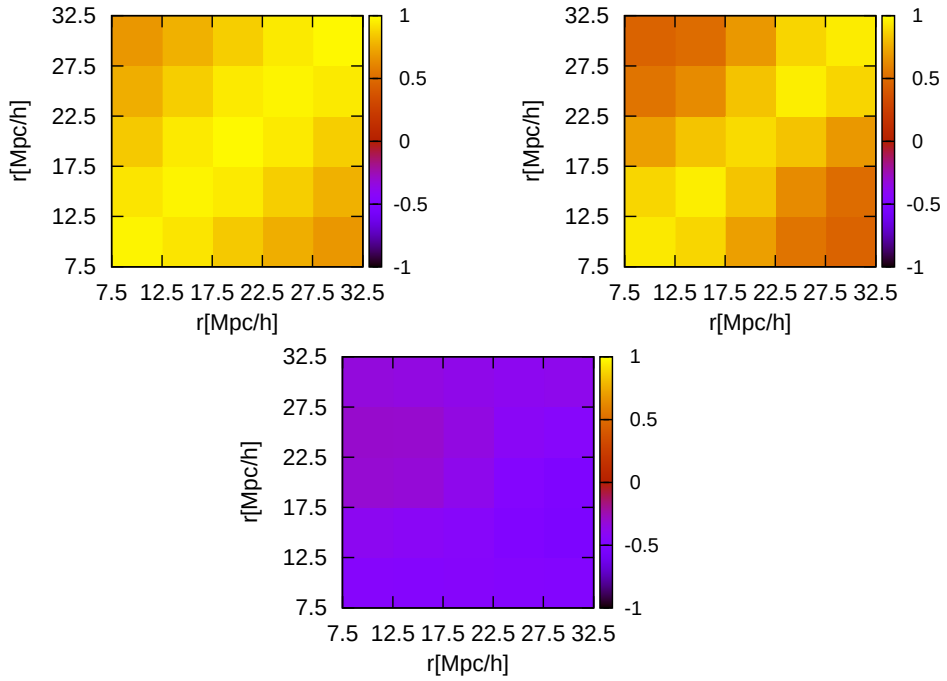

Figure 4.4: Reduced covariance matrix constructed for the monopole (top left panel) and quadrupole (top right panel) and the cross covariance between the two (bottom panel) in bins of $5\ \mathrm{Mpc}\ h^{-1}$.

will considered only the monopole and the quadrupole, where the most relevant information is contained, and ignore the contribution of the noisier subsequent orders. Figure 4.4 shows the reduced covariance matrix defined as $\tilde{C}_{i,j} = C_{i,j}/\sqrt{C_{i,i}C_{j,j}}$. We can see that there is significant off-diagonal covariance and non negligible covariance between monopole and quadrupole.

The mock data are analysed with a MCMC procedure, using the software package CosmoMC [49], which has been modified adding all the functions and parameters needed for our analysis. In particular we add a new module in which we implemented the model of the correlation function and we add parameters that were not already included in the code such as the distortions parameter β, the pairwise velocity dispersion σ_{12} and the bias factor b.

As we are going to see in the next sections we perform the likelihood analysis using both two-dimensional correlation function and its multipoles. In the recent literature we can find many works that exploit RSD to give constraints on the cosmological parameter using two-dimensional correlation function or its multipoles. For example, Contreras et al.

(2013) [16], Chuang & Wang (2012) [13] used the two-dimensional correlation function to estimate the growth rate and $H(z)$ and $D_A(z)$ respectively. de la Torre et al (2013) [22], Chuang et al. (2013) [12], Samushia et al. (2014) [64], Howlett et al. (2014) [37] instead made use of the multipoles to estimate the growth rate and other cosmological parameters.

The use of the multipoles has its pros and cons. They carry less information because they are constructed by integrating the two-dimensional correlation function. Moreover, with the two-dimensional correlation function it is possible to exclude the small scales from the analysis, which can cause problems due to the incorrect model of the non-linear motions. This is not fisible with the multipoles, because excluding the small scales in the integral (4.2) will give quantities that, by definition do not correspond to the multipoles anymore. However sometimes they are preferred because in this way it is possible to work with one dimensional quantities and this helps to reduce the noise in the covariance matrix. Indeed, as shown for instance by Hartlap et al (2007) [32], the numbers of bins used to measure the covariance matrix should be smaller than the number of mock catalogues, otherwise the covariance matrix turns out to be very noisy and this could lead to the underestimation of the parameter errors. In the worst case it could also give catastrophic problems such as very huge or negative values of the χ^2, which do not allow the convergence of the likelihood analysis procedure.

This is what happens in our case with the covariance matrix obtained from the two-dimensional correlation function, and for this reason we prefer to use the multipoles. Nevertheless we are going to show also some results obtained with the two-dimensional correlation function, which allowed us to check the mothod. Reducing to one dimensional quantities is not enough to ensure the convergence, and that is why we need to choose a suitable number of bins through the choice of the binning, which is set to $5\ \mathrm{Mpc}\ h^{-1}$. We refer to the Appendix A for further details.

However, even reducing the number of bins, in some cases numerical problems can still affect the parameter estimation. For this reason, following the approach of [13] we try to smooth the covariance matrix and use the smoothed version in our likelihood analysis. The smoothing algorithm exploits the fact that the diagonal elements of the matrix should be larger than the first off-diagonal elements, which in turn should be larger than all other elements. Therefore we consider the vector made up by the diagonal elements only and

average each of them using the two nearby elements according to the formula:

$$\tilde{C}(i,i) \quad = \quad (1 \; - \; p)C(i,i) \; + \; p\left[C(i+1,i+1) + C(i-1,i-1)\right]/m, \quad (4.14)$$

where p is a weight and m is the number of nearby elements considered in the averaging procedure, which is 2 in this case. If one of the two nearby elements is not present (i.e. when we considered the first and the last element of the vector) then $\tilde{C}(i,i) = C(i,i)$. The same algorithm is applied to the first off-diagonal elements, while the "generic" elements of the covariance matrix is averaged using all the nearby elements:

$$\tilde{C}(i,j) \;\; = \;\; (1 \; - \; p)C(i,j) \; + \; \frac{p}{m} \; \cdot \; \begin{bmatrix} C(i+1,j) + C(i-1,j) + \\ C(i,j+1) + C(i,j-1) + \\ C(i+1,j+1) + C(i-1,j-1) + \\ C(i+1,j-1) + C(i+1,j-1) \end{bmatrix}, \quad (4.15)$$

provided that both elements of each "couple" are present, otherwise only $m = \{2, 4, 6\}$ nearby elements can be used in the averaging procedure.

As we will see this smoothing procedure helps in alleviating some of the numerical problems related to the matrix noise, even if it does not work properly for all cases.

4.4 Reference value for the distortion parameter

Before measuring the amplitude of the redshift space distortions, we need to establish a reference value to which our measurements will be compared. The correct value of β for each sample can be obtained from the relation [55] [76]:

$$\beta(z) = \frac{\Omega_m^{0.55}(z)}{b(z)}\,, \quad (4.16)$$

where $\Omega_m^{0.55}(z)$ is the growth rate of fluctuations and $b(z)$ is the linear bias of the sample. The value of $\Omega_m(z)$ is computed via the relation:

$$\Omega_m(z) = \frac{(1+z)^3\Omega_{m0}}{(1+z)^3\Omega_{m0} + (1-\Omega_{m0})}\,. \quad (4.17)$$

The linear bias is estimated as $b^2 = \xi_{halo}(r)/\xi_{DM}(r)$. The values found are in agreement with the ones computed from two popular models: Sheth, Mo & Tormen (2001) [69] and Tinker et al. (2012) [73] (see [7, 52]).

For the BASICC simulation the present-day matter density is $\Omega_m(0) = 0.25$ and then, according to this equation, at redshift $z = 1$ we have $\Omega_m(1) = 0.73$. Therefore, for the catalogue we are going to use in the following tests, the bias factor is $b_t = 1.44$ and the corresponding value of the distortions parameter is $\beta_t = 0.58$.

4.5 Parameter estimation using the two-dimensional correlation function

The first test we perform aims at estimating the distortion parameter β using the two-dimensional correlation function, in order also to test the modules we add to CosmoMC.

We apply the method to the 27 mock catalogues, using for simplicity the diagonal covariance matrix. We run the MCMC analysis keeping all the parameter fixed to the input value of the simulation, with β and σ_{12} as the only free parameters, keeping the other parameters fixed to the input value of the simulation. We find $\bar{\beta} = 0.54 \pm 0.03$ and $\bar{\sigma}_{12} = 226.0 \pm 38.6$ km/s in the range of scales 3 Mpc $h^{-1} \leq r \leq 35$ Mpc h^{-1}. The value of β is underestimated with respect to the theoretical value of about 10%, in agreement with the results obtained by other works (see for instance [7]). This underestimation is due to fact that the model for the two-dimensional correlation function does not describe properly the non linear motions and improvements are needed (see [40, 54, 66, 74]). The values quoted here are obtained averaging the best fit values from the 27 mocks and the error is the scatter betweeen these values, which is one order of magnitude bigger than the error found by the MCMC for each mock. The best fit values for the 27 mocks are shown in Figure 4.5 together with the contour for one mock. The contours represent the 1σ and 2σ errors obtained with the MCMC procedure, which are clearly smaller than the scatter between the best fit points. This tells us that the covariance between bins can not be neglected in this case and that using only the diagonal matrix leads to an underestimation of the errors. This result will be confirmed in the following tests that make use of the multipoles. Moreover the contours can not reproduce the correlation between β and σ_{12}, which is expected from a theoretical point of view, since both parameter depend on the growth rate.

As next step we use the full covariance matrix obtained from the two-dimensional correlation function. In the range of scales analysed we use 33 bins for each direction to measure the correlation function, so that the covariance matrix dimension is 1089×1089. However, having only 27 sub-boxes makes the covariance matrix too noisy, indeed using the full covariance matrix leads to unconverging results. Even the smoothing procedure does not solve the problem, leading to biased results for each mock catalogue.

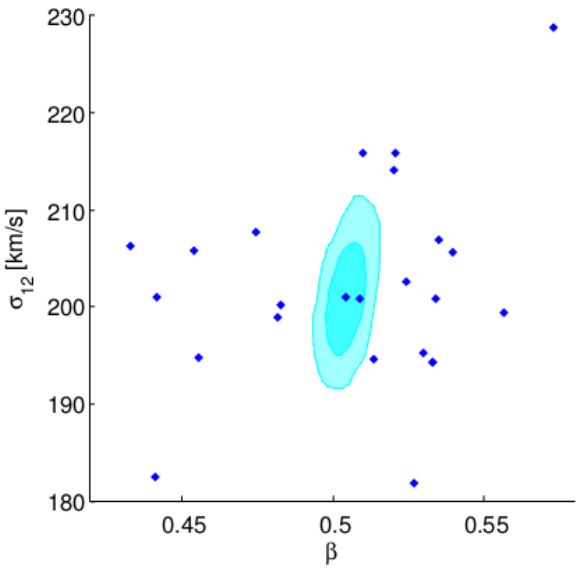

Figure 4.5: Contour plot for one of the mock catalogues (cyan ellipses) and the best fit values from the 27 mocks (blue diamonds) obtained with the two-dimensional correlation function and its diagonal covariance matrix. The ellipses represent 1 and 2σ contours.

4.6 Estimation of β using correlation function multipoles

We apply the MCMC procedure using now the multipoles of the correlation function, measured in bins of 5 $\mathrm{Mpc}\ h^{-1}$, using both the diagonal and the full covariance matrix. At first we measure only the distortion parameter β, keeping σ_{12} fixed to a suitable value. This choice is made for sake of simplicity and to speed up the computation, since we are more insterested in testing the method and the covariance matrix rather than in the estimate of β. We obtain $\bar{\beta} = 0.48 \pm 0.01$ with the full matrix and $\bar{\beta} = 0.52 \pm 0.01$ with the diagonal matrix. We can see that the best fit value for β are different with respect to the ones found in the previous case, and this result is quite obvious, since σ_{12} is fixed to the same value for all the mock catalogues. Indeed, due to the correlation between these two parameters, fixing σ_{12} to a given value, which can not be the best fit value for a certain mock, can bias the estimate of the β parameter. However, choosing a different value of σ_{12} will change the best fit values but not the amplitude of their errors, as verified.

Once also the multipole method has been tested, we can run our code to estimate simultaneously β and σ_{12}. What we find is $\bar{\beta} = 0.54 \pm 0.02$ and $\bar{\sigma}_{12} = 235.7 \pm 7$ km/s

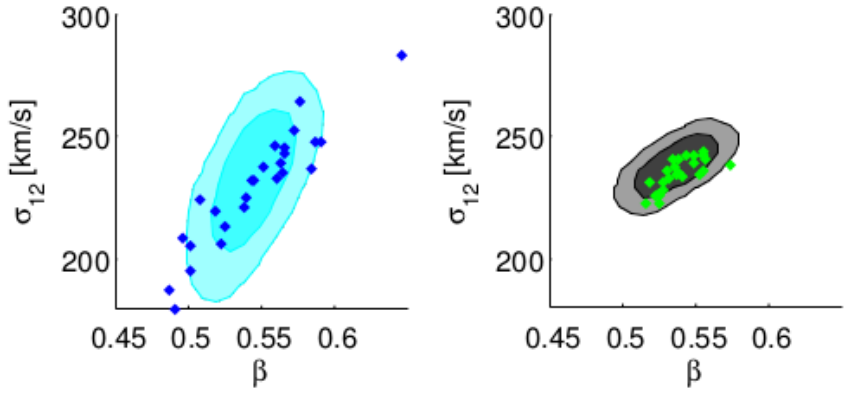

Figure 4.6: Contour plot for one mock catalogue (cyan and black ellipses) and the best fit for the 27 mocks (blue and green diamonds) obtained using the multipoles of the correlation function with the diagonal matrix (left panel) and the full matrix (right panel) with β and σ_{12} as free parameters. The ellipses represent 1 and 2σ contours.

using the full matrix and $\bar{\beta} = 0.55 \pm 0.02$ and $\bar{\sigma}_{12} = 233.0 \pm 17.8$ km/s with the diagonal matrix. These results are summarized in Figure 4.6, which shows the contours for one mock catalogue and the best fit points for each mock catalogue, for both diagonal and full matrix. We can notice again that the error obtained with the diagonal matrix is underestimated with respect to the scatter between the 27 best fit values, and that this does not happen when we use the full matrix. The discrepancy between scatter and mean error is now around 50%, smaller than the one obtained with the two-dimensional correlation function. This result lets us think that the amplitude of the discrepancy can be related to the dimension of the covariance matrix, in particular to the ratio between the number of bins and the number of mock catalogues. Indeed it seems that the smaller the ratio is, the smaller the discrepancy is.

4.7 Estimation of β and bias factor b

In all these tests we always kept the bias factor fixed to the theoretical value obtained via equation (4.16). However, in a real survey it is not possible to estimate the bias factor b through equation (4.16) since the real observable is the correlation function of galaxies, whereas ξ_{DM} can not be directly observed. A possible solution is to assume a model for the dependence of the bias on the mass of groups or clusters, which can be estimated for

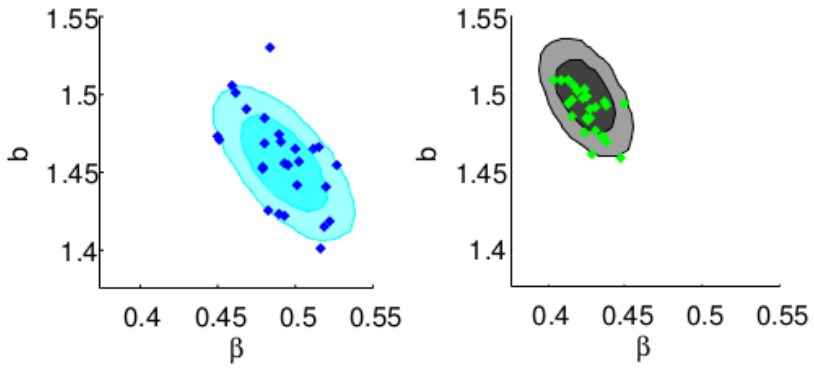

Figure 4.7: Contour plot for one mock catalogue (cyan and black ellipses) and the best fit for the 27 mocks (blue and green diamonds) obtained using the multipoles of the correlation function with the diagonal matrix (left panel) and the full matrix (right panel) with β and b as free parameters. The ellipses represent 1 and 2σ contours.

instance from the X-ray emission temperature or luminosity. Due to these uncertainties on the bias factor we prefer to consider it a free parameter. This is the convenient choice when we want to estimate other cosmological parameters, such neutrino mass fraction, that affect the amplitude of the correlation function.

The results obtained from the MCMC procedure with β and b as free parameters are $\bar{\beta} = 0.43 \pm 0.01$ and $\bar{b} = 1.49 \pm 0.01$ using the full matrix and $\bar{\beta} = 0.49 \pm 0.02$ and $\bar{b} = 1.46 \pm 0.02$ with the diagonal matrix only. They are shown in Figure 4.7, where we can observe the comparison between the single mock error represented by the contour plot, and the scatter of the best fit values obtained from the 27 mocks.

The discrepancy between the values of β is due to having fixed the value of σ_{12} and can be removed letting this parameter free to vary. Indeed repeting the analysis adding σ_{12} as a free parameter, we obtain (for one single mock catalogue) $\beta = 0.58 \pm 0.04$ and $b = 1.38 \pm 0.02$ with the full matrix and $\beta = 0.53 \pm 0.03$ and $b = 1.40 \pm 0.02$ with the diagonal matrix. The best fit now are in agreement within 2σ, and, as expected to happen with one more free parameter in the MCMC, the error of the two parameter is bigger than the previous case.

The results of all these tests ensure the validity of the method and the accuracy of the changes made on CosmoMC. They are the starting point for a broader analysis which will

lead to the main results of this thesis.

Chapter 5

Statistical and sistematic errors in RSD measurements

The aim of this thesis is to exploit RSD plus power spectrum shape to constrain cosmological parameters through a MCMC procedure, and to make forecasts of the statistical precision reachable in future projects, aimed at measuring these parameters. Some attempts have been recently made to produce forecasts based on RSD using numerical simulations. For example, as explained in Chapter 2, Guzzo et al. [29] used mock surveys extracted from the Millennium simulation to estimate the errors affecting their measurements of the growth rate. They found a scaling relation for the relative error on the β parameter as a function of survey volume and mean density (see eq. (2.32)).

This formula has been refined by Bianchi et al. [7] in 2012. The authors analysed the same catalogues of dark matter haloes used in this thesis, extracted from a snapshot of the BASICC simulation [4] at $z = 1$, finding that the parameter β is underestimated by up to 10%, depending on the minimum mass of the considered haloes. They proposed a new fitting formula, that aims at separating the dependence of the error on bias and density:

$$\frac{\delta\beta}{\beta} \approx C b^{0.7} V^{-0.5} \exp\left(\frac{n_0}{b^2 n}\right) \tag{5.1}$$

where $n_0 = 1.7 \cdot 10^{-4}\, h^3 \mathrm{Mpc}^{-3}$ and $C = 4.9 \cdot 10^2\, h^{-1.5} \mathrm{Mpc}^{1.5}$.

Here we want to follow the same approach to study the error dependence for some different parameters, focusing our attention on the neutrino mass fraction. The differences with respect to the work made in [7] mainly reside on the fact that we use a theoretical real space correlation function obtained from the dark matter power spectrum instead of the deprojected one, in the use of the multipoles of the correlation function rather than the full two-dimensional correlation function, and in the procedure used to estimate parameters,

N_{part}	M_{cut} $[h^{-1}\,M_{\odot}]$	$\mathcal{N}_{tot}$	n $[h^3\,\mathrm{Mpc}^{-3}]$
20	1.10×10^{12}	7483318	3.11×10^{-3}
63	3.46×10^{12}	2164960	9.00×10^{-4}
136	7.47×10^{12}	866034	3.60×10^{-4}
236	1.30×10^{13}	423511	1.76×10^{-4}
364	2.00×10^{13}	230401	9.58×10^{-5}

Table 5.1: Properties of the halo catalogues used in the analysis. N_{part} is the minimum number of particles per halo; M_{cut} is the corresponding threshold mass; $\mathcal{N}_{tot}$ is the number of haloes with $M_{halo} \geq M_{cut}$; n is the number density, computed as $\mathcal{N}_{tot}/V$ where $V = 1340^3 h^{-3}\mathrm{Mpc}^3$ is the simulation volume.

which in our case is an MCMC likelihood analysis. In this way we can provide constraints on cosmological parameters using the shape of the power spectrum and also map their probability distributions.

In a companion paper of [7], Marulli et al. (2012) [52] investigated other effects that could impact the measurement of RSD. In particular they studied how redshift measurements errors and geometrical distortions affect RSD. They found that large redshift errors introduce a systematic bias in the estimate of β which can be alleviated using a Gaussian model for the velocity distribution function $f(v)$, rather than the exponential one. They also found that the measure of β can be affected by the geometric distortions induced by the incorrect choice of the background cosmology, when converting redshifts into distances. However this effect is very small and the correct value of β can be recovered even assuming a wrong cosmological model, that is assuming a different value for the matter density parameter Ω_m.

5.1 Halo catalogues from the BASICC simulation

To reach our goal we are going to apply the method described in Chapter 4 to a series of halo catalogues characterized by different values of bias, density and volume extracted from the BASICC simulation.

We consider the snapshot of the BASICC simulation at $z = 1$ and select halo catalogues with different mass thresholds (i.e minimum numbers of particles per halo). The properties of these catalogues are summarized in Table 5.1. This selection allows us to study the dependence of the error on the sample bias. However, samples with high bias are also less dense. Therefore, in order to separate the dependence of the errors on bias and density, the

		$M_{cut} \times 10^{-12}$ $[h^{-1}\ M_\odot]$				
		1.10	3.46	7.47	13.0	20.0
	6.87	$*$	$*$	$*$	$*$	$*$
	9.68	$*$	$*$	$*$	$*$	$*$
	12.1	$*$	$*$	$*$	$*$	
	17.6	$*$	$*$	$*$	$*$	
	24.8	$\circ$	$\circ$	$\circ$		
$n \times 10^5$	36.0	$*$	$*$	$*$		
$[h^3\,\mathrm{Mpc}^{-3}]$	58.7	$*$	$*$			
	90.0	$\circ$	$*$			
	131	$*$				
	204	$*$				
	311	$\circ$				
		1.44	1.80	2.15	2.49	2.89
				bias		

Table 5.2: Sub-samples used in our analysis to explore the dependence of the errors on mean density, bias and volume. Each sample is characterized by given values of mean density and bias (or mass threshold). The full, non-diluted, samples coincide with the bottom entry of each column. The entries in the table identified by circles represent the sample used to test the dependence of the errors on volume. For these samples the simulation box has been splitted in N^3 sub-boxes with $N = \{3, 4, 5, 6\}$, whereas for the other sub-samples (asterisks) we only consider $N = 3$.

samples have been diluted to create a series of catalogues with decreasing density, down to a value of $6.87 \times 10^{-5} h^3$ Mpc^{-3} for which shot noise starts to dominate [7]. For each of these samples with varying bias and density, we split the simulation box in N^3 sub-boxes, with $N = 3$, obtaining 27 sub-boxes. For some samples we also split the box in N^3 parts with $N = \{4, 5, 6\}$ in order to explore the error dependence on volume, as shown in Table 5.2.

Then we extract the mock catalogues and measure the correlation function using the Landy&Szalay estimator [45]. The covariance matrix is computed for each sub-samples according to the procedure described in Section §4.3.

In this Chapter we are going to show some preliminary results obtained analysing all the 11 sub-samples from the catalogue with $M_{cut} = 1.10 \times 10^{12}\ h^{-1} M_\odot$, corresponding to the first column of Table 5.2.

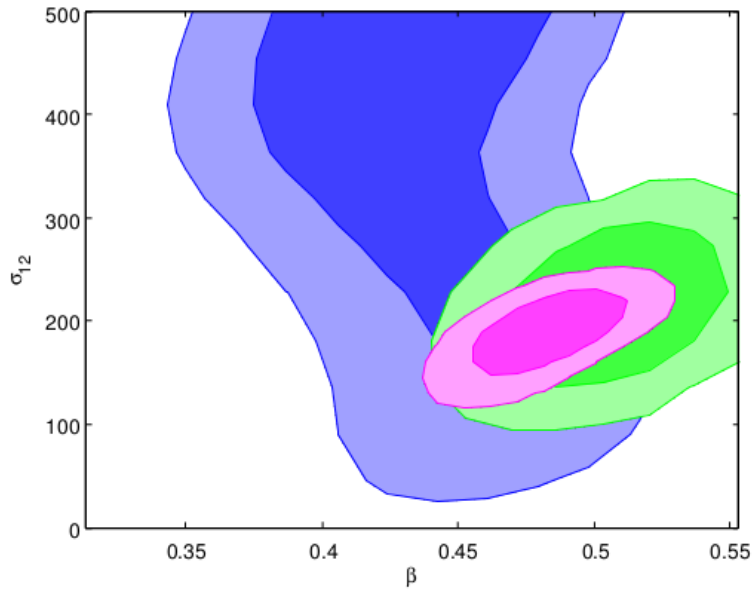

Figure 5.1: Contour plot for β and σ_{12} obtained using the monopole only (blue contours), the quadrupole only (green contours) and both monopole and quadrupole (magenta contours). The ellipses represent 1σ and 2σ contours.

5.2 Results on the error dependence

In order to study the dependence on density of the relative β error, we perform the MCMC analysis on the sub-samples obtained diluting the original catalogue with $M_{cut} = 1.10 \times 10^{12}\ h^{-1}\ M_{\odot}$, considering β and σ_{12} as free parameters, and keeping all the other parameters fixed to the input value of the simulation.

In Figure 5.1 we plot, for a single mock catalogue, the contours obtained using the monopole and the quadrupole separately in the MCMC likelihood analysis, plus the contour obtained using monopole and quadrupole. We can see that when using the monopole only we are not able to estimate the σ_{12} value, since the non-linear effects are mostly embedded in the quadupole. The contours obtained using both multipole moments lie, as expected, on the intersection of the contours from monopole and quadrupole. In Figure 5.2 we show the 1σ and 2σ contours obtained using both monopole and quadrupole, for the same mock catalogues, considering this time different density values, with larger contours corresponding lower densities.

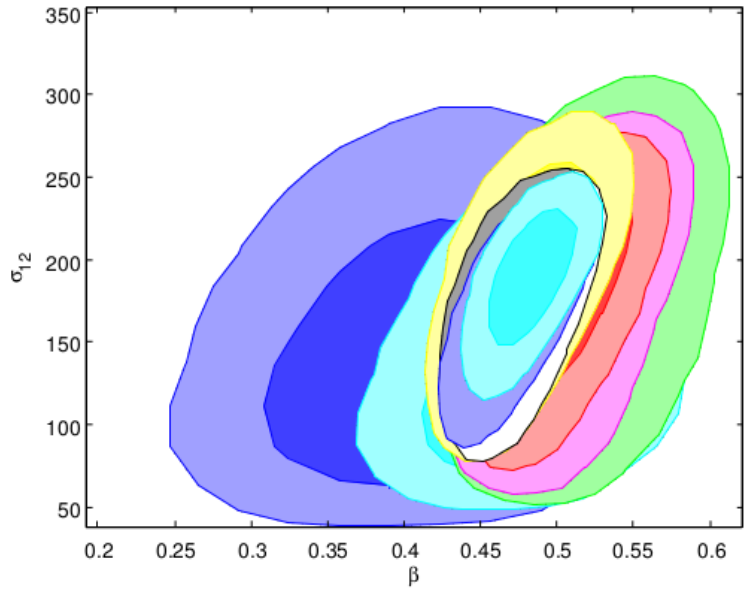

Figure 5.2: Contour plot for β and σ_{12} from catalogues with increasing density, larger contours correspond to lower densities. The ellipses represent 1σ and 2σ contours.

This result is summarized in Figure 5.3, where it is shown the relative error on β as a function of density. The dots represent the mean error over the 27 mock catalogues, for each density value, and the error bars represent the scatter between the 27 errors.

The dot-dashed line represents a fitting function having the same functional form adopted by Bianchi et al. (2012) [7]:

$$\frac{\delta\beta}{\beta} \propto \exp\left(\frac{n_0}{An}\right), \tag{5.2}$$

with $A \simeq 1.6$. The parameter n_0 is fixed to $1.7 \times 10^{-4}\ h^3$ Mpc^{-3} which is roughly the density at which cosmic variance starts to dominate. We want to stress that we are not interested in performing such a detailed study on σ_{12} since the model does not properly describe the non-linear motion, thus it is just treated as a fitting parameter.

The same analysis has been performed considering β and b as free parameters. In Figure 5.4 we present the results obtained using separately the monopole and the quadrupole compared to the ones obtained with both vectors. As in the previous case we can notice that the two parameters can not be constrained accurately using only one multipole at a time.

The results obtained using monopole and quadrupole together, considering mock cata-

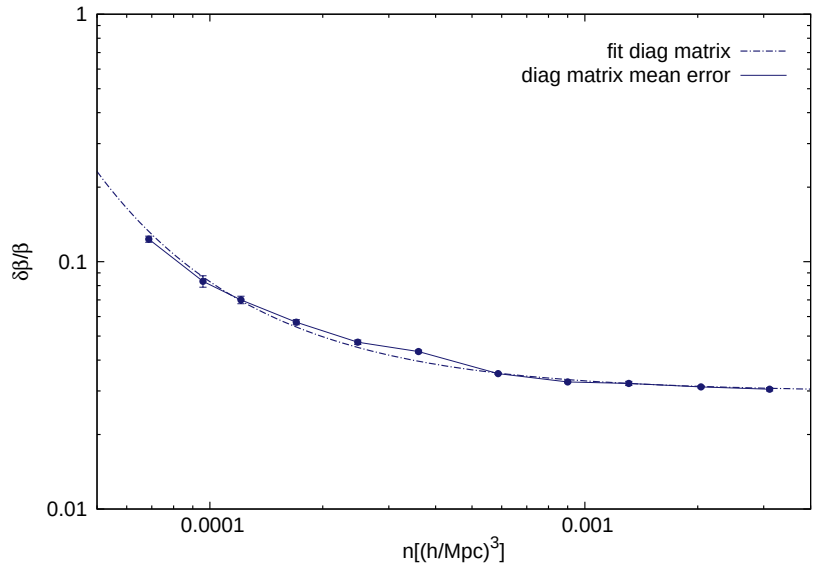

Figure 5.3: Mean relative error on β over the 27 mocks (blue dots connected by solid line) as a function of density, obtained with the diagonal matrix analysing the mocks with β and σ_{12} as free parameters. The dot-dashed line represents the fitting function described by equation (5.2). The error bars represent the scatter between the 27 errors.

logues with different density values, are shown in Figure 5.5 in the form of contour plot. In Figure 5.6 we plot the errors for β and b as a function of density. The conclusions we can draw from this analysis are very similar to the ones reached in the previous case. Indeed, both error trends can be represented analytically with the fitting function of equation (5.2).

This basically confirms the trend observed by [7], even if the fitting parameters are different. This is not fully expected since the results have been obtained with different methods, using also different parameters in some cases, and small differences can be present.

5.3 Assessing the validity of the matrices

We repeat the analysis using also the full matrix and the smoothed one obtained through the algorithm described in section §4.3, in order to establish whether we can trust the full matrix and whether the smoothing is a necessary step or not.

As in the previous section, we consider at first the case with β and σ_{12} as free parameters. The results are shown in Figure 5.7. What we expect is that the error computed using the smoothed matrix lies between the ones obtained with the diagonal and the full matrix, since the algorithm aims at smoothing out the numerical fluctuations reducing the

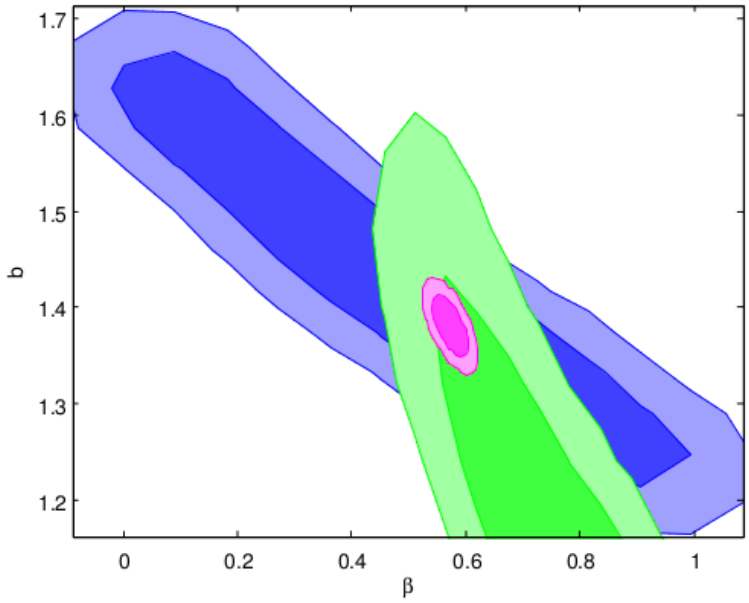

Figure 5.4: Contour plot for β and b obtained using the monopole only (blue contours), the quadrupole only (green contours) and both monopole and quadrupole (magenta contours). The ellipses represent 1σ and 2σ contours.

off-diagonal elements.

The results of the analysis with β and b as free parameters are illustrated in Figure 5.8 for the relative error on β and b. As regards β, the smoothed matrix gives an error which is smaller than both the full and the diagonal matrices, for almost all the density bins. The opposite trend is observed for the relative error on b, that is with the smoothed matrix we can infer an error which is bigger than the ones obtained with the diagonal and the full matrices.

Due to the tension of the resuts obtained with the smoothed matrix, we can conclude that the smoothing procedure is not reliable. We can also draw the conclusion that even the error obtained with the full matrix is not trustworthy. Indeed, as it can be noticed from the Figures 5.7 and 5.8, the full matrix sometimes gives an error which is smaller than the one obtained with the diagonal matrix. This is exactly the problem pointed out by Hartlap et al. (2007) [32], which is related to the relation between the number of bins and the number of mock catalogues, as already explained in section §4.3 of Chapter 4. These reasonings, together with the fact that the diagonal matrix allows to obtain a less scattered trend for the

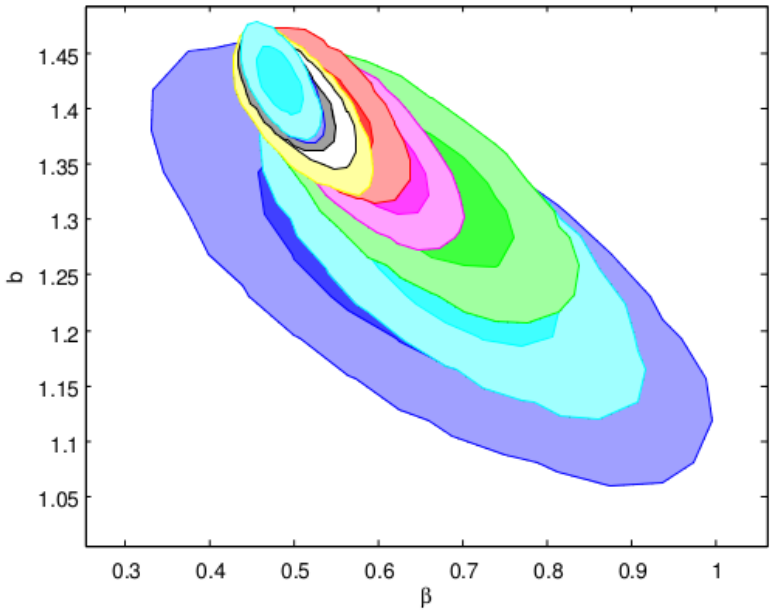

Figure 5.5: Contour plot for β and b from catalogues with increasing density, larger contours correspond to lower densities. The ellipses represent 1σ and 2σ contours.

error in all the cases analysed, lead us to exclude from our subsequent analyses the full and the smoothed matrices, so we are going to make use of the diagonal matrix only.

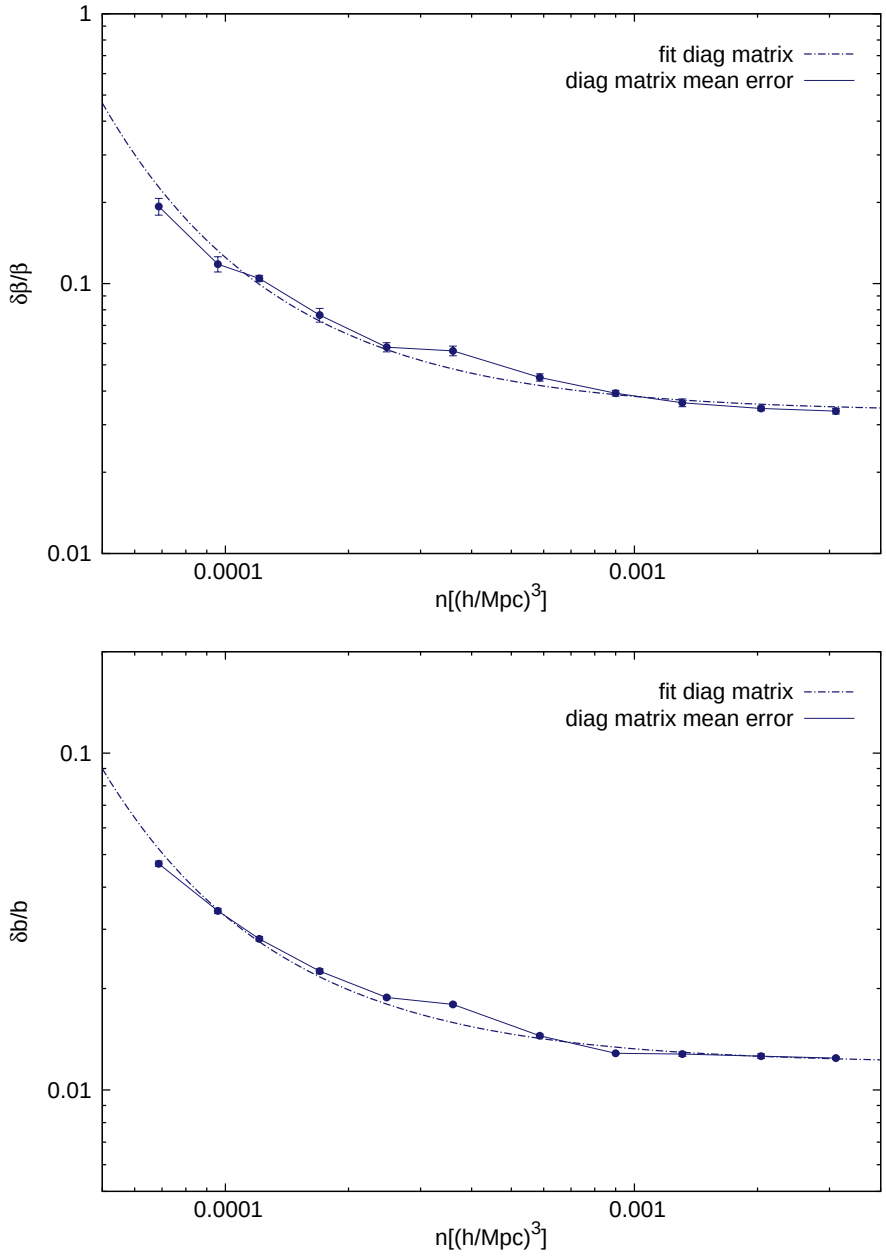

Figure 5.6: Mean relative error on β (upper panel) and b (lower panel) over the 27 mocks (blue dots connected by solid line) as a function of density, obtained with the diagonal matrix analysing the mocks with β and b as free parameters. The dot-dashed line represent the fitting function of equation (5.2). The error bars represent the scatter between the 27 errors.

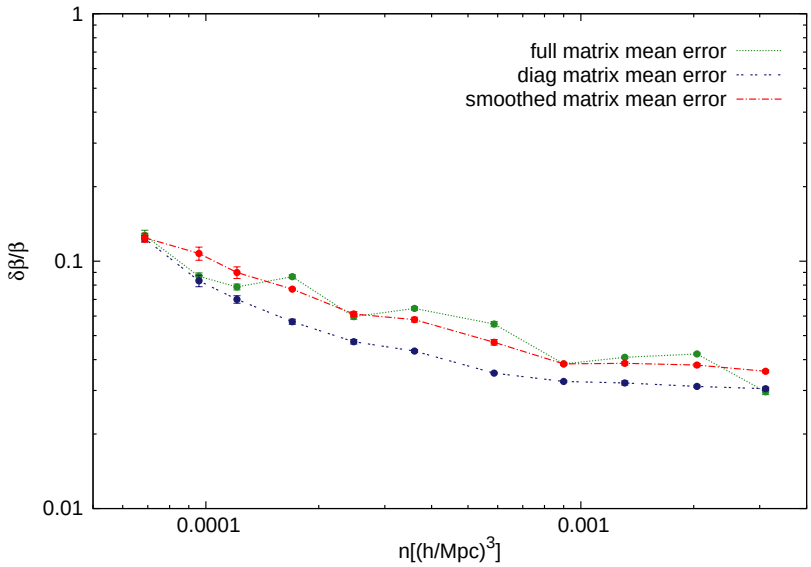

Figure 5.7: Relative error on β as a function of density obtained analysing the mock data with β and σ_{12} as free parameters. The dots represent the mean MCMC error over the 27 mocks, for the diagonal (blue dots connected by the dashed line), the full matrix (green dots connected by the dotted line) and the smoothed matrix (red dots connected by the dot-dashed line). The error bars represent the scatter between the 27 errors.

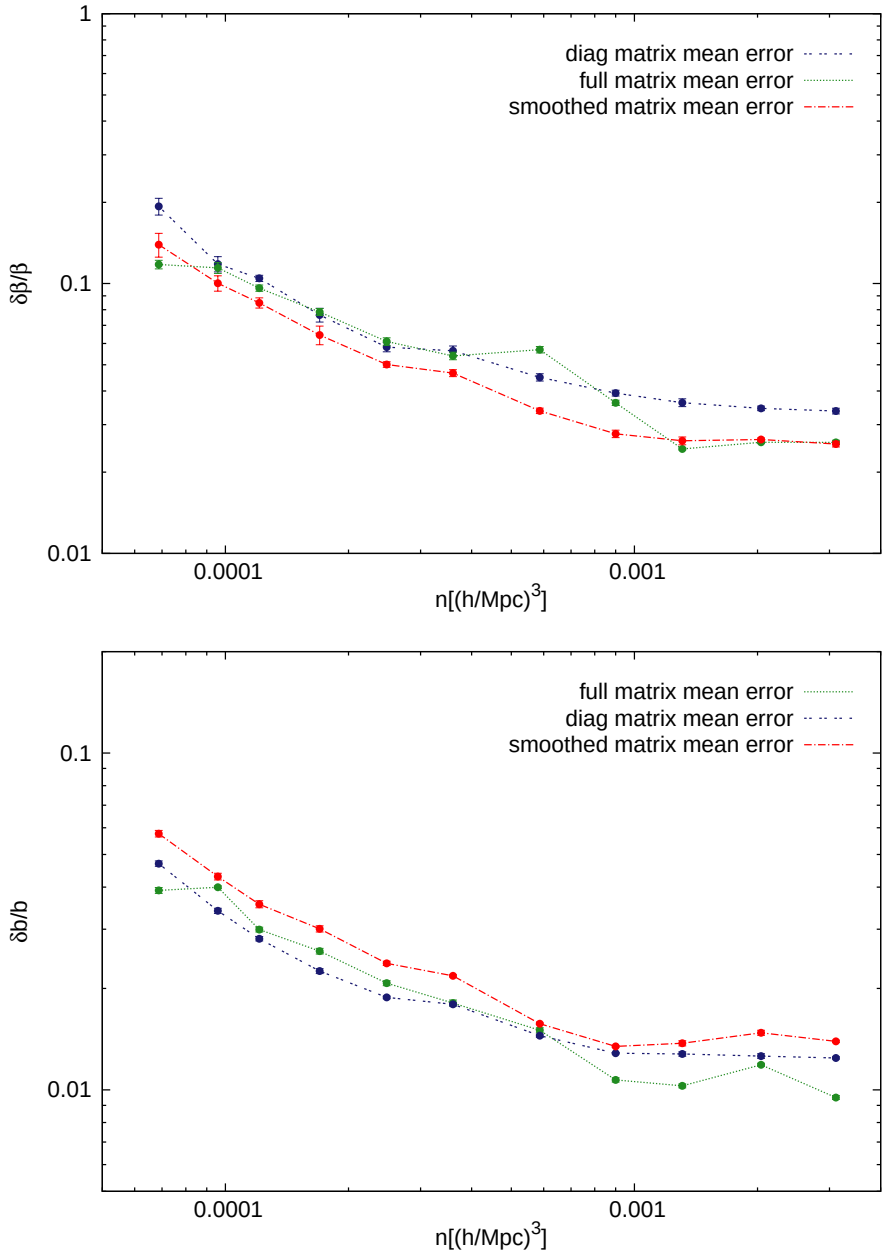

Figure 5.8: Relative error on β (upper panel) and b (lower panel) as a function of density obtained analysing the mock data with β and b as free parameter. The dots represent the mean MCMC error over the 27 mocks, for the diagonal (blue dots connected by the dashed line), the full matrix (green dots connected by the dotted line) and the smoothed matrix (red dots connected by the dot-dashed line). The error bars represent the scatter between the 27 errors.

Chapter 6

Constraining the neutrino mass fraction

Estimating the neutrino mass is one of the main challenge for cosmology today. According to the standard model of particles, neutrinos are massless, weakly interacting, particles. However the experiments on the oscillations of solar and atmospheric neutrinos started some years ago tell us that neutrinos cannot be massless. Neutrino oscillations experiments are sensitive to the mass differences between neutrino eigenstates, and the current data imply $|\Delta m^2_{31}| \simeq 2.4 \times 10^{-3}\mathrm{eV}^2$ and $\Delta m^2_{21} \simeq 27.6 \times 10^{-5}\mathrm{eV}^2$ ([5]). From these mass differences it is possible to construct two mass hierarchies for neutrinos: the so-called "normal" hierarchy, $m_1 < m_2 \ll m_3$, with two light neutrinos and a heavy one and the "inverted" hierarchy, $m_3 \ll m_1 < m_2$, with only one light neutrino and two heavy ones. These measurements provide a lower limit for the sum of neutrino masses of $\approx 0.06\mathrm{eV}$ (see [47] for a review).

However oscillation experiments can only measure the differences in the squared masses of the neutrinos and not the absolute mass scale. Now that cosmology has entered in the precision era and the cosmological parameters can be constrained at percent level, observations of the universe can assist in the quest for neutrino mass, since neutrinos affect the evolution of the universe in several observable ways.

6.1 Effects of neutrinos on large scale structure

After thermal decoupling, relic neutrinos constitute a collisionless fluid, where the individual particles free-stream with a characteristic velocity which is the thermal velocity. As long as neutrinos are relativistic, the free-streaming scale is simply the Hubble radius. When they

become non-relativistic, their thermal velocity decays and the free-streaming scale is equal to [47]:

$$k_{FS} = 0.82 \frac{H(z)}{(1+z)^2} \frac{m_\nu}{1\mathrm{eV}} \, h \, \mathrm{Mpc}^{-1} \, . \tag{6.1}$$

The physical effect of free-streaming is to damp neutrino density fluctuations on scale $k > k_{FS}$, where neutrinos can not cluster due to their large thermal velocity. This affects the matter power spectrum since neutrinos do not contribute to the gravitational potential wells produced by dark matter and baryons. Hence the power spectrum is reduced by a factor $(1 - f_\nu)^2$, where

$$f_\nu \equiv \frac{\Omega_\nu}{\Omega_m} \tag{6.2}$$

is the neutrino mass fraction. For the same reason, the growth rate of dark matter perturbations is suppressed and acquires a scale dependence as demonstrated by [43].

Neutrino mass has non-trivial effects also on features of the CMB temperature anisotropies. Indeed neutrino mass can alter the redshift of matter-radiation equality if $\Omega_m h^2$ is fixed, and viceversa. The first case translates in an overall modification of the amplitude and the location of the acoustic peaks. A change in the matter density would instead affect the angular diameter distance to the last scattering surface $D_A(z_{dec})$, and the slope of the CMB spectrum at low multipoles due to the Integrated Sachs-Wolfe effect.[1]

Many works attempted to measure neutrino mass combining different cosmological probes: [67], [35], [36], [20], [60], [65], [72], [39], [44], [63], [77]. One of the latest constraints come from [6]: combining measurements from the Baryon Oscillation Spectrscopic Survey (BOSS) CMASS DR11 with WMAP9 they found $\sum m_\nu = 0.36 \pm 0.14\mathrm{eV}$ which excludes massless neutrinos at 2.6σ. The significance of this measurement is increased to 3.3σ including weak lensing and BAO measurements.

Among large scale structure probes, RSD are one of the most promising ways to measure the neutrino mass. Indeed, in presence of massive neutrinos, the parameter β depends not only on redshift, but also on the wavenumber, because of the scale dependence acquired by the growth rate $f(k, z)$. The suppression of the growth rate affects also the rms of galaxy peculiar velocity, since both the growth rate $f(k, z)$ and the matter power spectrum enter in the bulk flow predicted by linear theory ([43], [23]).

Massive neutrinos strongly affect also the spatial clustering of cosmic structures: as

[1] The Integrated Sachs-Wolfe effect describes the energy change of the CMB photons as they pass through a gravitational potential well.

shown by [53], the average number density of massive structures is suppressed with an enhanching of the halo bias in a ΛCDM plus neutrinos with respect to a ΛCDM model without neutrinos. This implies a rise in the halo correlation function due to the smaller value of the distortion parameter and the bulk flow in presence of massive neutrinos. Therefore the best fit value of β and σ_{12} are reduced by an amount that increases with $\sum m_\nu$ and z.

However, all these effects are degenerate with the amplitude of the matter power spectrum, described by σ_8. Indeed, the differences between the best fit values of β in a ΛCDM and a $\Lambda\mathrm{CDM} + \nu$ models is significantly reduced if the two cosmologies are normalized to the same value of σ_8. Nonetheless, the relative difference between the theoretical values of β in these two models, at $z = 1$, is $\delta\beta/\beta \simeq 3\%$ which corresponds to the precision reachable by future redshift surveys in measuring the redshift space distortion parameter at $z \leq 1$.

This means that RSD can contribute to estimate the total neutrino mass, helping to disentagle degeneracies with the other cosmological parameters.

6.2 Estimate of the neutrino mass fraction

We analyse the mock data with the MCMC procedure. Here the parameter space that we explore is made up by three parameters: the neutrino mass fraction $f_\nu = \Omega_\nu/\Omega_m$, the bias parameter b and the pairwise velocity dispersion σ_{12}. The neutrino mass fraction enters the model through the shape of the theoretical undistorted correlation function. The bias instead enters in the model twice: first when converting the real space DM correlation function into the halo correlation function through the usual procedure $\xi_{halo}(r) = b^2\xi_{DM}(r)$ and then in the multipole expansion through the parameter β, which in our analysis is expressed as $\Omega_m^\gamma(z)/b(z)$, with $\gamma = 0.55$ according to [50]. $\Omega_m(z)$ is the input value of the simulation computed at redshift $z = 1$ via the equation (4.17).

Once the theoretical correlation function is computed from a certain set of cosmological parameters, it must be rescaled to the fiducial cosmology used to measure the correlation function, which in our case is the input cosmology of the simulation, according to the relation (see [68]):

$$\xi_{th}^{fid}(r_p, \pi) = \xi_{th}\left(\frac{D_A(z)}{D_A^{fid}(z)} r_p, \frac{H^{fid}(z)}{H(z)}\pi\right) . \tag{6.3}$$

Indeed geometrical distortions can be introduced due to the incorrect choice of the back-

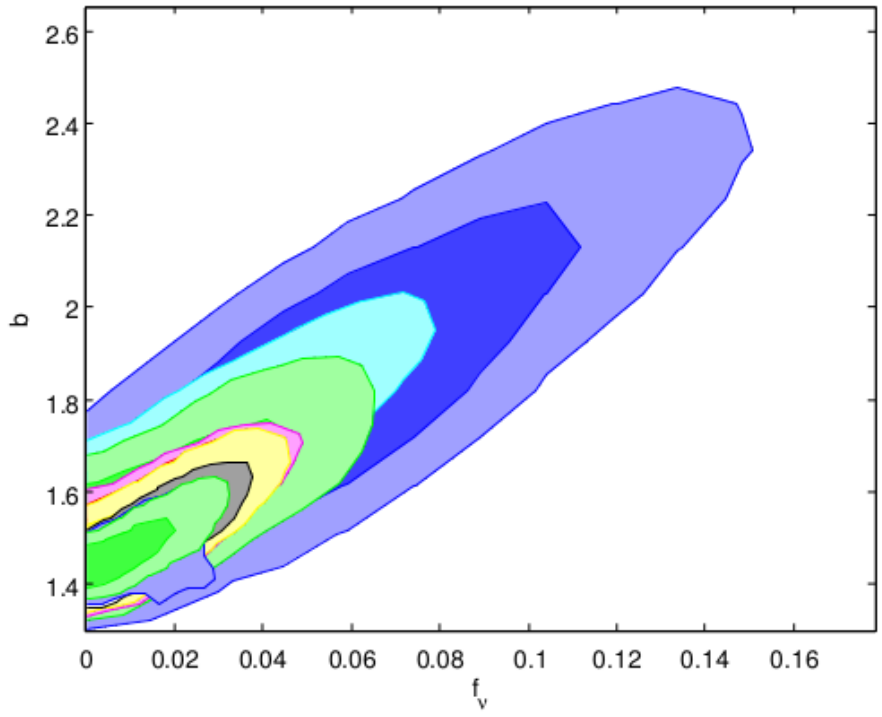

Figure 6.1: Contour plot for b and f_ν for the catalogue with $M_{cut} = 1.20 \times 10^{12}\ M_\odot\ h^{-1}$. Larger contours correspond to lower density samples. The input value of simulation are recovered within 1σ.

ground cosmology when converting redshifts into distances. However, in our case this procedure is not necessary since the only varying cosmological parameter is f_ν whereas the total amount of matter Ω_m is held fixed to the input value of the simulation, so that $H(z)$ and $D_A(z)$ do not change and there are no geometric distortions to be accounted for.

The joint constraints on the neutrino mass fraction f_ν and bias b obtained from the catalogues with $M_{cut} = 1.20 \times 10^{12}\ M_\odot\ h^{-1}$ are shown in Figure 6.1. We can see that the correct values of both parameters are recovered for each catalogue.

We obtained these results using the monopole and the quadrupole of the correlation function, neglecting the first two bins of the quadrupole moment. Indeed, using the monopole together with the whole quadrupole, we found a sistematic underestimation of the bias factor for the samples characterized by high bias values. This is probably due to the fact that the model does not properly describe small scales and this makes impossible to recover the correct values of the parameters.

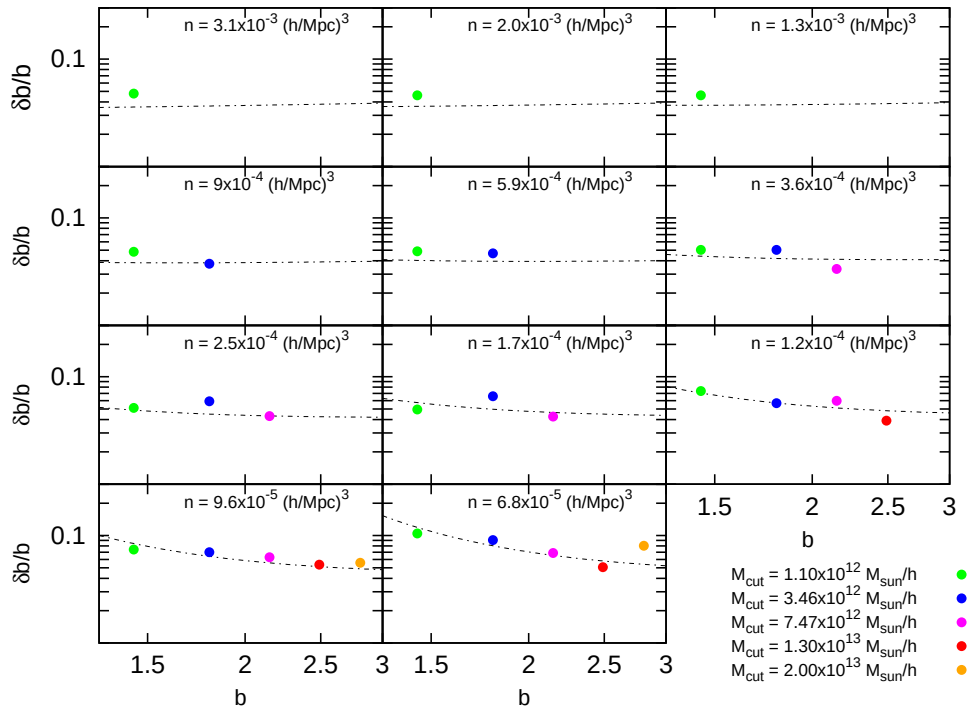

Figure 6.2: Bias relative errors as a function of bias for different mass and density samples, obtained from a single mock catalogue. The dots represent the errors measured from the simulated samples, the dashed lines show the scaling formula obtained by fitting our results (equation 6.8).

6.3 Error dependence on the survey parameters

Having analysed all the samples from Table 5.2 we can now present our results about the dependence of the b and f_ν errors on the three survey parameters: bias, density and volume. We illustrate at first the dependence on one parameter at a time, and then we summarize these dependencies presenting a fitting formula able to describe the overall behaviour of the errors.

6.3.1 Error dependence on bias

In Figures 6.2 and 6.3 we plot the relative errors on b and f_ν, respectively, as a function of bias, in different density bins. For all the sample considered the volume is held fixed. The error dependence on bias is basically constant in the range of density $1.7 \times 10^{-4}\ (h/\mathrm{Mpc})^3 <$

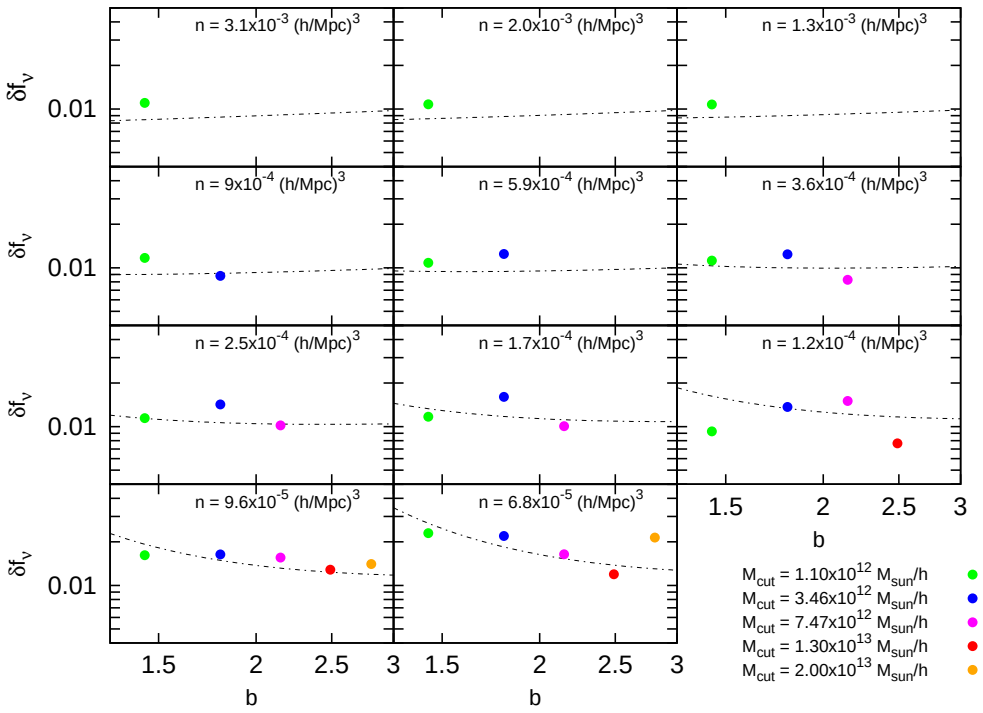

Figure 6.3: Errors on neutrino mass fraction as a function of bias for different mass and density samples, obtained from a single mock catalogue. The dots represent the errors measured from the simulated samples, the dashed lines show the scaling formula obtained by fitting our results (equation 6.8).

$n < 3.1 \times 10^{-3}\ (h/\mathrm{Mpc})^3$. For density smaller than $1.7 \times 10^{-4}\ (h/\mathrm{Mpc})^3$ instead, the error tends to decrease as the bias increases. In the high density regime, the trend of the error can be described by a power law of the form [7]:

$$\delta x \propto b^{\alpha_1}\ , \tag{6.4}$$

where the exponent α_1 will have a very small value. In the low density regime, that is below $1.7 \times 10^{-4}\ (h/\mathrm{Mpc})^3$, the dependence seems to be better described by an exponential decrease [7]:

$$\delta x \propto \exp(1/b^{\alpha_2})\ . \tag{6.5}$$

These results suggest that at high density the samples give similar errors. At low densities, the gain due to a high distortion signal of the low-bias samples is cancelled out by the dilution of the catalogues. The high-bias samples instead, which are characterized by a

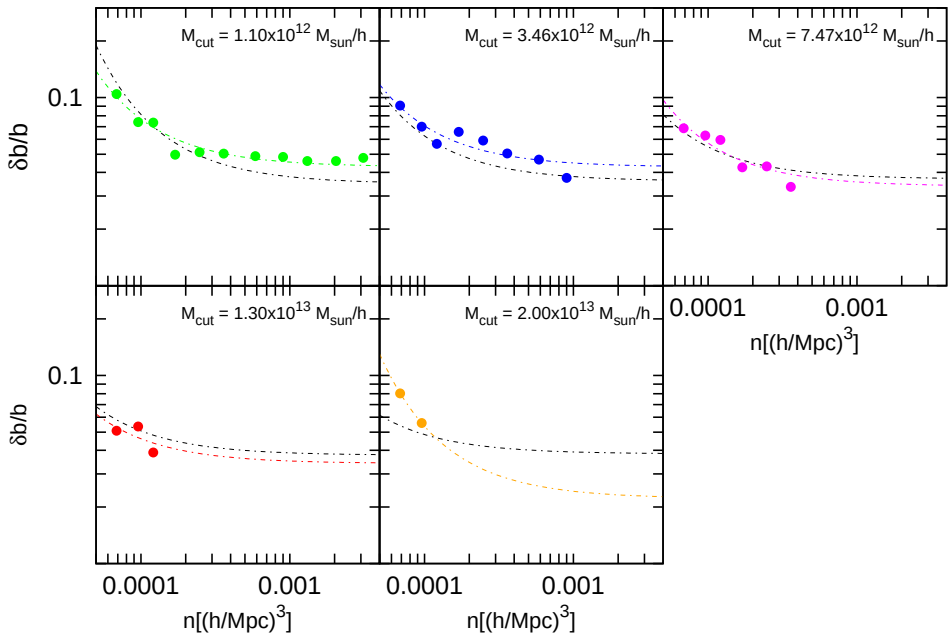

Figure 6.4: Bias relative errors as a function of density for different mass (i.e. bias) samples, obtained from a single mock catalogue. The dots represent the errors measured from the simulated samples. The coloured dashed lines represent the fitting function of equation (6.8) for each mass sample. The black dashed lines instead show the scaling formula obtained by fitting all the catalogues simultaneously. The colour code is the same of the previous Figures.

stronger clustering signal and are intrinsically less dense, give a smaller error and then are more suitable when estimating these parameters using RSD.

6.3.2 Error dependence on density

The dependence of the errors on density is represented in Figures 6.4 and 6.5 for b and f_ν respectively. We plot the errors for samples of different values of bias and density, having fixed the volume. Both errors clearly decrease in an exponential way, becoming constant for high values of the density. Indeed decreasing the density leads to a larger error, because of the shot noise, whereas going at higher densities there is a dominance of the cosmic variance and the error remains almost constant. This behaviour can be described by an esponential

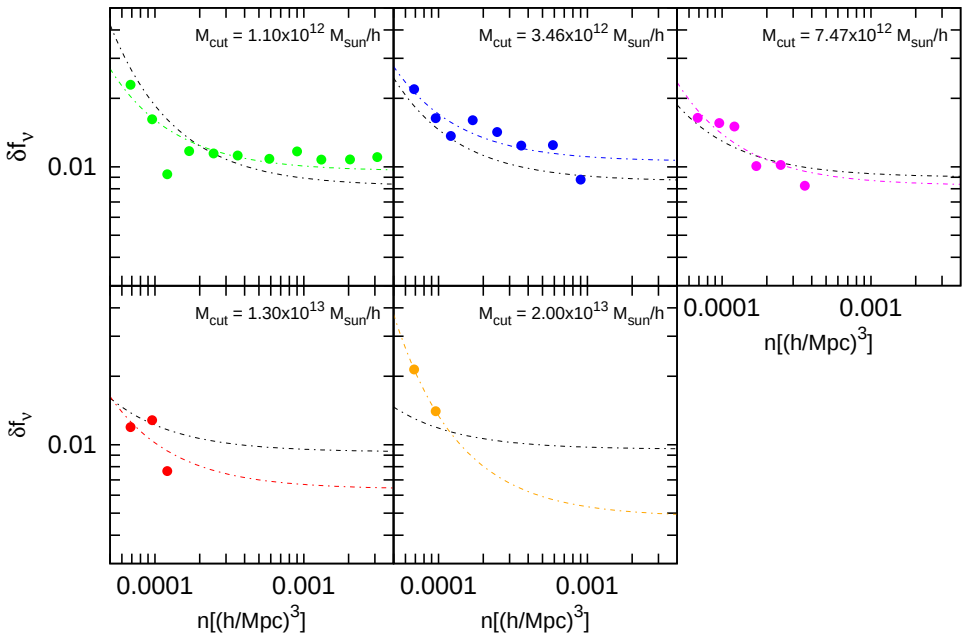

Figure 6.5: Errors on neutrino mass fraction as a function of density for different mass (i.e. bias) samples, obtained from a single mock catalogue. The dots represent the errors measured from the simulated samples. The coloured dashed lines represent the fitting function of equation (6.8) for each mass sample. The black dashed lines instead show the scaling formula obtained by fitting all the catalogues simultaneously. The colour code is the same of the previous Figures.

function of the form:

$$\delta x \propto \exp(n_0/n) \,, \tag{6.6}$$

where n_0 is the density value that separates the shot noise regime from the cosmic variance one. We can notice that this exponential decrease depends also on bias, with a flattening of the exponential function for the high-bias samples, reflecting what already seen in the previous section. Therefore it is more appropriate to describe these errors with a function which is a combination of the function (6.5) and (6.6) [7]:

$$\delta x \propto \exp(n_0/nb^{\alpha_2}) \,. \tag{6.7}$$

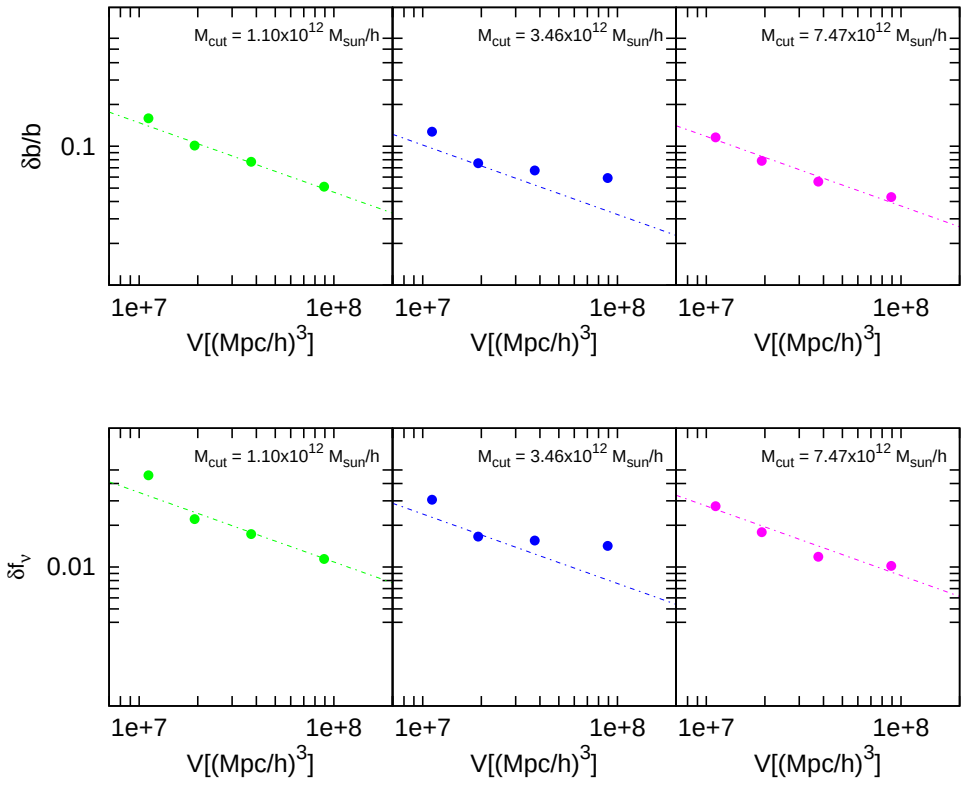

Figure 6.6: Bias relative errors (upper panel) and errors on neutrino mass fraction (lower panel) as a function of volume, obtained from a single mock catalogue. As in the previous figures the dots represent our measurements and the dashed lines show the fitting formula (6.8).

6.3.3 Error dependence on volume

Finally we illustrate the dependence on volume. We consider 5 sub-samples of different bias and density and for each of them we split the cube of the simulation in N^3 cubes with $N = \{4, 5, 6\}$ in order to reduce the volume of the catalogues. We applied the same method as before and computed the mean errors for each sub-samples. We find that the errors scale as the inverse of the square root of the volume, irrespective of bias and density, confirming the dependence found by [29] and [7]. The results are shown in Figure 6.6, where we plot the measurements from catalogues with different volume and bias, for a fixed density value.

6.3.4 Fitting formula for the overall error dependence

According to these considerations, we try to fit the errors with the functional form [7]:

$$\delta x \approx C b^{\alpha_1} V^{-0.5} \exp\left(\frac{n_0}{b^{\alpha_2} n}\right), \tag{6.8}$$

finding a good agreement with our measurements. The best-fit parameters are $C = 311\ h^{-1.5}$ Mpc$^{1.5}$, $\alpha_1 = 0.1$ and $\alpha_2 = 1.9$ for the relative error on b, whereas for the error on f_ν we find $C = 72\ h^{-1.5}$ Mpc$^{1.5}$, $\alpha_1 = 0.2$ and $\alpha_2 = 2$. In both cases $n_0 = 1.7 \times 10^{-4}\ h^3$ Mpc^{-3} which is roughly the density at which cosmic variance starts to dominate. We want to stress the fact that the error that we fit is the relative error for b and the absolute error on f_ν, therefore in the fitting formula (6.8) δx should be replaced with $\delta b/b$ and δf_ν respectively. The overall behaviour of the error as a function of bias and density at a fixed volume is summarized in Figure 6.7, while Figure 6.8 shows the comparison between data and function.

We have found a fitting function able to describe the amplitude of the errors on bias and neutrino mass fraction as a function of density, bias and volume, which are three typical parameters of a redshift survey. As explained in Chapter 4, the use of the diagonal covariance matrix leads to slightly underestimate the error so one can think that these results could be biased. However we expect that the effect of the full covariance matrix can be simply absorbed by the normalization constant C, because the covariance elements of the matrix should affect in the same way all the samples, shifting the errors above or below the values found with the diagonal matrix.

The predictive power of this formula makes possible to forecast the precision reachable in measuring these two parameters: given the volume of a survey, together with the density and the bias of its target, it is possible to estimate the error that can be obtained when analysing the data using the same approach described in this thesis. For example, a Euclid-like survey should be able to measure the neutrino mass fraction with a precision of $\approx 2 \times 10^{-4}$ in a volume of $\approx 4.2 \times 10^9$ centered at redshift $z = 1$ with $\Delta z = 0.2$, considering a galaxy sample with bias ≈ 1.13 and density $\approx 17 \times 10^{-3}$. This value is of the same order of magnitude of the one quoted for the sum of neutrino masses in the Euclid Red Book [46], obtained with the Fisher Matrix method for BAO measurements, which is $\delta M_\mu \approx 0.03$eV. According to the relation $\Omega_\nu = M_\nu/(h^2 93.8\text{eV})$, it translates in an accuracy on the neutrino mass fraction of the order of $\approx 10^{-4}$.

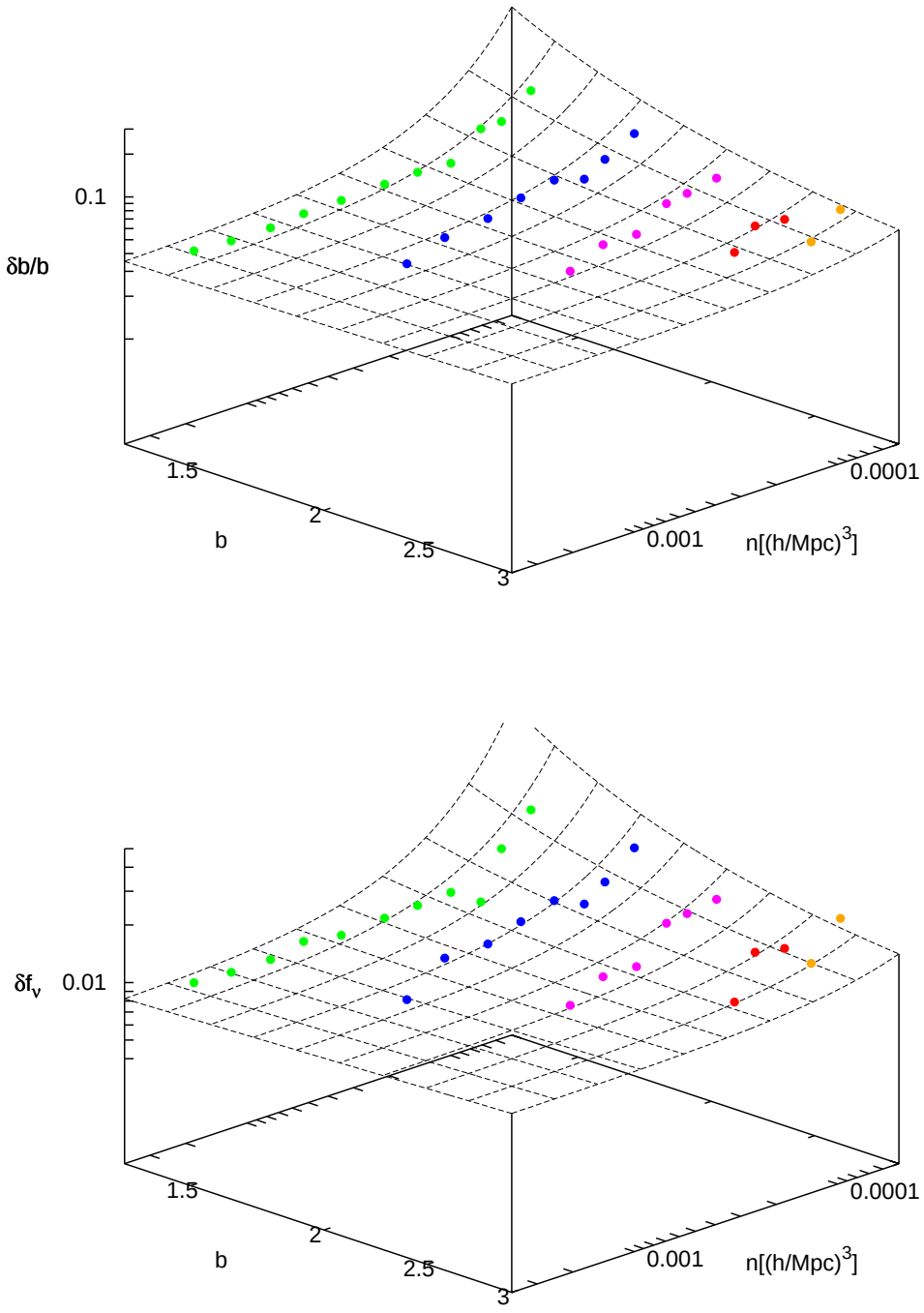

Figure 6.7: Errors on bias (upper panel) and on neutrino mass fraction (lower panel) as a function of density and bias overplotted on the surface described by the fitting formula of equation (6.8)

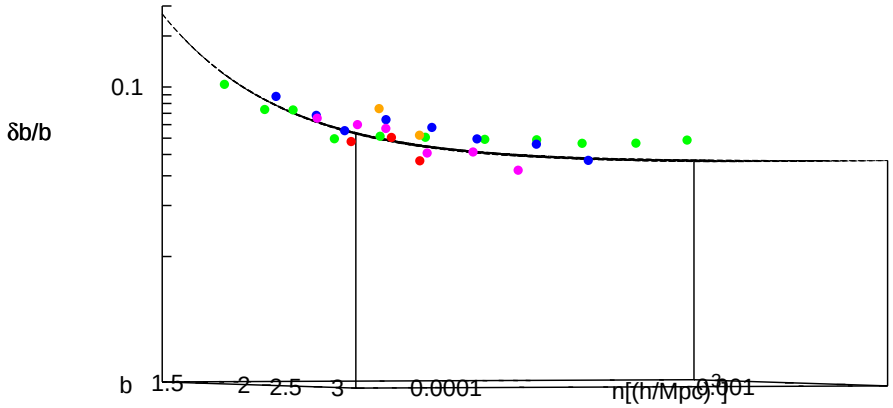

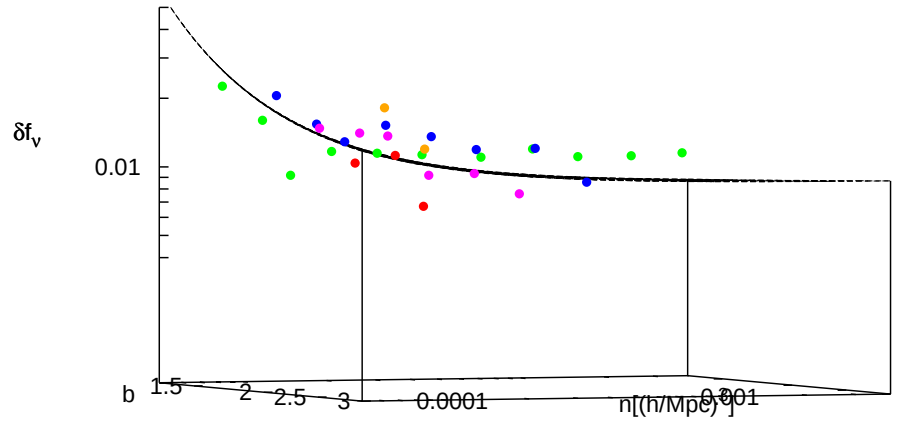

si

Figure 6.8: Errors on bias (upper panel) and on neutrino mass fraction (lower panel) as a function of density and bias. The plots are the same as the ones in Figure 6.7 except for the fact that the plots are oriented in order to show the agreement between our measurements and the fitting function.

Conclusions

In this thesis we have presented a powerful method to estimate cosmological parameters based on measurements of RSD, analysed with a MCMC likelihood analysis. We have measured the multipoles of the correlation function in bins of $5\mathrm{Mpc}\ h^{-1}$, up to a scale of $35\mathrm{Mpc}\ h^{-1}$, from mock data extracted from the halo catalogues of the BASICC Simulation at $z = 1$. The halo catalogues have been selected in order to have different values of bias, density and volume, which are three fundamental parameters used to describe a redshift survey. This selection has allowed us to perform a broad analysis of the statistical errors that occur in measuring cosmological parameters, studying how these errors depend on the survey parameters.

A crucial point in this method is represented by the covariance matrix, which assesses the errors of the correlation function. We have performed a detailed study of the matrix estimated from the mock catalogues, performing the MCMC analysis using the diagonal, the full and the smoothed matrix. According to the results obtained from catalogues of varying density, we have established that the diagonal matrix is the more trustworthy, even if the errors on the parameters, that come as a results of the MCMC procedure, turn out to be a little underestimated. Indeed the number mock catalogues at our disposal were not sufficient to construct a reliable full covariance matrix which is affected by numerical issues that a smoothing procedure is not able to fully remove.

The method has been applied to measure the neutrino mass fraction f_ν and the bias parameter b, but it is quite general and can be applied to estimate other cosmological parameters. We have found that the estimates of f_ν and b are in agreement with the input values of the simulation within 1σ. For what concerns the error trend as a function of density, volume and bias, we have found that our measurements are fitted to a good approximation by the scaling formula given in equation (6.8) for both b and f_ν, with just small differences in the fitting parameters. This formula allows us to to assess the precision reachable on

measurements of f_ν and b, based on RSD, quoting an error of $\approx 2 \times 10^{-4}$ for the neutrino mass fraction and $\approx 2 \times 10^{-3}$ for the bias factor for a Euclid-like survey. We think that these results are not biased by the use of the diagonal matrix, since the contribution of the full matrix can be described by a simple renormalization of the fitting function. We stress that the fitting formula is valid at redshift $z = 1$, and further studies must be carried out in order to generalize it, even if there is no obvious reason that the dependence on parameters should change with redshift.

Appendix A

Optimizing the choice of the bin size

We measured the multipoles of the correlation function in bins of $5\ \mathrm{Mpc}\ h^{-1}$, since this binning helps us to reduce the noise in the covariance matrix. Here we briefly review the reasons that bring us to this choice.

We are interested in studying the behaviour of the parameter errors as a function of the typical survey parameters such as density, bias and volume. Therefore, in order to choose a suitable binning for the multipoles we analyse 11 subsamples of different densities obtained diluting the catalogue from the BASICC simulation with $M_{cut} = 1.1.0 \times 10^{12}\ h^{-1}\ M_{\odot}$, with β as the only free parameter.

A binning of $1\ \mathrm{Mpc}\ h^{-1}$ has been immediately excluded since in this case we have 33 bins for each multipoles and then a covariance matrix dimension of 66×66, which still leads to unconverging results when using the full matrix.

Then the analysis has been performed using bins of 3 and $5\ \mathrm{Mpc}\ h^{-1}$ using both the diagonal and the full covariance matrices.

The results obtained with a $3\ \mathrm{Mpc}\ h^{-1}$ binning are summarized in Figure A.1, which shows the relative error of β as a function of density obtained with the diagonal and the full matrices. Each dot represents the mean error over the 27 mocks. From the figure it is clear that even if the MCMC converges to a certain best fit value, the full matrix still carries some numerical problems. Indeed the error obtained with the full matrix appears to be very scattered with respect to the one obtained with the diagonal matrix and there is no physical reason that justifies this behaviour. So this leads us to think that the results obtained with the full matrix are driven by numerical issues.

This hypotesis is confirmed by the result obtained using bins of $5\ \mathrm{Mpc}\ h^{-1}$. They are shown in Figure A.2, together with the error obtained with $3\ \mathrm{Mpc}\ h^{-1}$ binning, both with

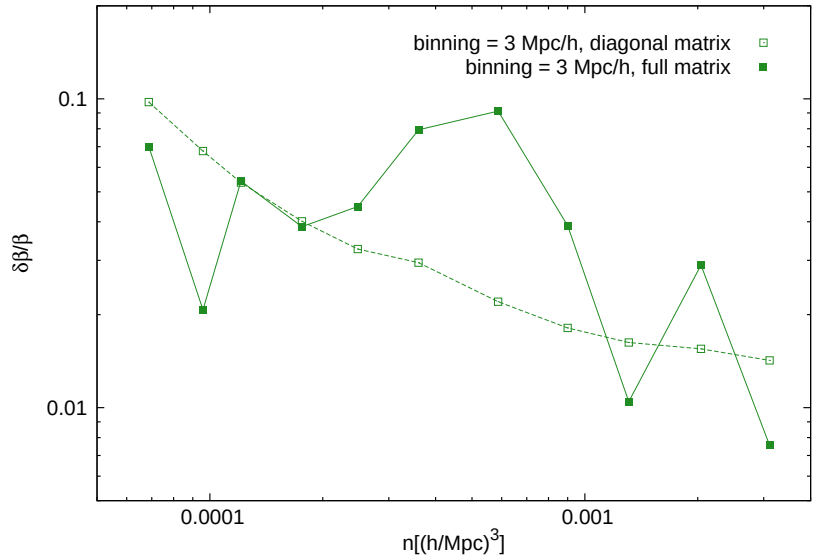

Figure A.1: Relative error on β as a function of density obtained using the diagonal matrix (empty squares) and the full matrix (full squares). The dots represent the mean value of the error over the 27 mocks of each samples.

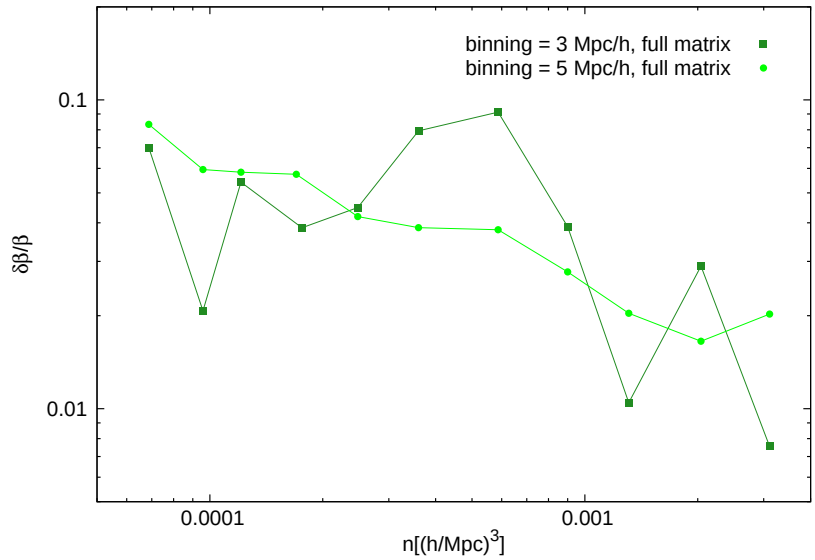

Figure A.2: Relative error on β as a function of density obtained using the full covariance matrix with bin size $3\ \mathrm{Mpc}\ h^{-1}$ (squares) and $5\ \mathrm{Mpc}\ h^{-1}$ (dots). It is evident the improvements in the results when using a larger bin size.

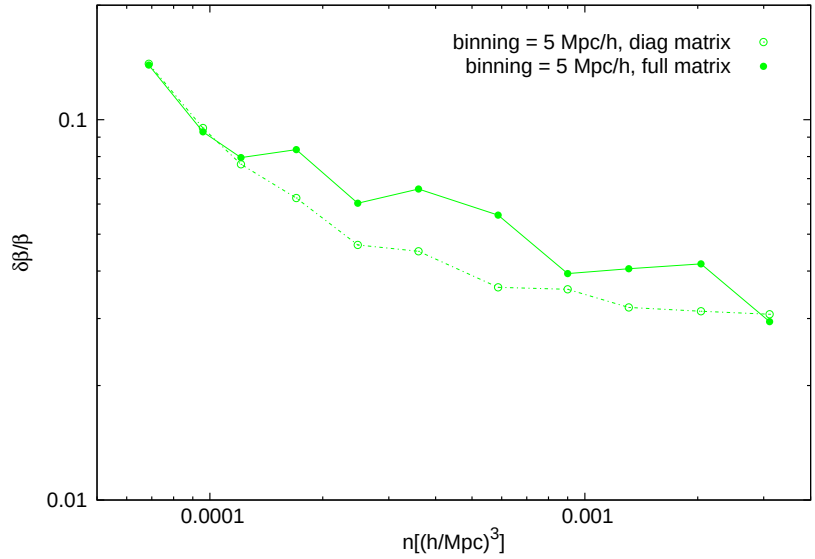

Figure A.3: Relative error on β as a function of density obtained using the diagonal matrix (empty dots) and the full matrix (full dots). The bin size is $5\ \mathrm{Mpc}\ h^{-1}$ and β and σ_{12} are considered as free parameters.

the respective full matrix. It is evident that increasing the bin size alleviates the numerical problems since the error turns out to be less scattered.

To confirm these results we performed the same analysis letting also σ_{12} free to vary. The Figure A.3 shows the comparison between the errors obtained with the diagonal and the full matrix and highlights again that the numerical issues can be kept under control with a suitable choice of the bin size.

Larger bin size will cause loosing to much information on the correlation function, so $5\ \mathrm{Mpc}\ h^{-1}$ will be our definitive choice.

Bibliography

[1] Abramo, L.R. and Finelli, F., Phys. Rev. D, 64, 083513 (2001).

[2] Alcock C., Paczynski B., Nature, 281, 358 (1979).

[3] Amendola, L., et al., Cosmology and Fundamental Physics with the Euclid Satellite, Living Rev. Relativity, 16 (2013).

[4] Angulo, R.E., et al., MNRAS, 383, 755 (2008).

[5] Beringer J. et al., [Particle Data Group Collaboration], Phys. Rev. D 86, 010001 (2012).

[6] Beutler, F., et al., MNRAS, Volume 444, 3501 (2014).

[7] Bianchi, D., et al., MNRAS, 427, 2420 (2012).

[8] Brans, C., Dicke, R.H., Physical Review, 124, 925 (1961).

[9] Cabré, A., Gaztañaga, E., MNRAS, 393, 1183 (2009).

[10] Caldwell, R.R., Dave, R. and Steinhardt, P.J., Phys. Rev. Lett., 80, 1582 (1998).

[11] Christensen, N., Meyer, R., Phys. Rev. D, 64, 022001 (2000).

[12] Chuang C. H. et al., eprint arXiv:1312.4889

[13] Chuang C. H., Wang Y., MNRAS, 426, 226 (2012).

[14] Chuang C. H., Wang Y., MNRAS, 431, 2634 (2013).

[15] Chuang C. H., Wang Y., MNRAS, 435, 255 (2013).

[16] Contreras, C. et al., MNRAS, 430, 924 (2013).

[17] Copeland, E.J., Sami, M. and Tsujikawa, S., Int. J. Mod. Phys. D 15, 1753 (2006).

[18] Davis M., Efstathiou G., Frenk C. S., White S. D. M., ApJ, 292, 371, (1985).

[19] Davis, M.; Peebles, P. J. E., ApJ, 267, 465, (1983).

[20] Dunkley, J. et al. [WMAP Collaboration], Astrophys. J. Suppl. 180, 306 (2009).

[21] Dvali, G., Gabadadze, G., Porrati, M., Phys. Lett. B, 485, 208, (2000).

[22] de la Torre, S., & VIPERS Team, A&A, 557, A54 (2013).

[23] Elgarøy, Ø., Lahav, O., New Journal of Physics, 7, 61 (2005).

[24] Esposito-Farese, G. and Polarsky, D., Phys Rev. D, 63, 063504 (2001).

[25] Fisher K. B., Davis M., Strauss M. A., Yahil A., Huchra J. P., MNRAS 267, 927 (1994).

[26] Gannouji, R., Polarsky, D., Ranquet, A. and Starobinsky, A.A., JCAP, 9, 16 (2006).

[27] Gelman, A., Rubin, D., Statistical Science, 7, 457 (1992).

[28] Gilks, W. R., Richardson, S., Spiegelhalter, D. J., Markov Chain Monte Carlo in Practice, Chapman & Hall, (1996).

[29] Guzzo, L., et al., Nature, 451, 541 (2008).

[30] Hamilton A. J. S., ApJ, 385, L5 (1992).

[31] Hamilton A. J. S., ApJ, 417, 19 (1993).

[32] Hartlap, J., Simon, P., Schneider, P., A&A, 464, 399 (2007).

[33] Hawkins, E., et al., MNRAS, 346, 78 (2003).

[34] Hewett, P. C., MNRAS, 201, 867, (1982).

[35] Hinshaw, G. et al. [WMAP Collaboration], Astrophys. J. Suppl. 180, 225 (2009).

[36] Hinshaw, G., Larson, D., Komatsu, E. et al., ApJS, 208, 19 (2013).

[37] Howlett, C., Ross, A. J., Samushia, L., Percival, W. J., Manera, M., arXiv:1409.3238v1 (2014).

[38] Hu, W., Eisenstein, D. J., Tegmark, M., Phys. Rev. Lett., 80, 5255 (1998).

[39] Ichiki K., Takada M., Takahashi T., Phys. Rev. D 79, 023520 (2009).

[40] Jennings E., Baugh C. M., Pascoli S., MNRAS, 410, 2081 (2011).

[41] Kaiser, N., MNRAS, 227, 1 (1987).

[42] Kerscher, M., Szapudi, I., Szalay, A. S., ApJ, 535, L13 (2000).

[43] Kiakotou, A., Elgarøy, Ø., Lahav, O., 2008, Phys. Rev. D, 77, 063005

[44] Komatsu E. et al. [WMAP Collaboration], Astrophys. J. Suppl. 192, 18 (2011).

[45] Landy S. D., Szalay A. S., ApJ, 412, 64 (1993).

[46] Laureijs, R., et al., Euclid Definition Study Report, arXiv:1110.3193 (2011).

[47] Lesgourgues J., Pastor S., Phys. Rept. 429, 307 (2006).

[48] Lewis, A., Challinor, A., Lasenby, A., ApJ, 538, 473 (2000).

[49] Lewis, A., Bridle, S., Phys. Rev. D, 66, 103511 (2002).

[50] Linder E. V., Phys. Rev. D, 72, 043529 (2005).

[51] Ma, C.P., and Bertschinger, E., Astrophys. J., 455, 7 (1995).

[52] Marulli F., Bianchi D., Branchini E., Guzzo L., Moscardini L., Angulo R. E., MNRAS, 426, 2566 (2012).

[53] Marulli, F., Carbone, C., Viel, M., Moscardini, L., Cimatti, A., MNRAS, 418, 346 (2011).

[54] Okumura T., Jing Y. P., ApJ, 726 (2011).

[55] Peebles P. J. E., Large-Scale Structure of the Universe (1980).

[56] Perlmutter, S. et al. [Supernova Cosmology Project Collaboration], 1999, Astrophys. J., 517, 565.

[57] Planck Collaboration, Planck 2013 results. XVI. Cosmological parameters, eprint arXiv:1303.5076.

[58] Pons-Bordería, M. J., Martinez, V. J., Stoyan, D., Stoyan, H., Saar, E., ApJ, 523, 480 (1999).

[59] Press W. H., Teukolsky S. A., Vetterling W. T., Flannery B. P., Numerical Recipes: The Art of Scientific Computing, Third Edition (2007).

[60] Reid B. A., Verde L., Jimenez R., Mena O., JCAP, 01, 003 (2010).

[61] Riess, A.G., et al. [Hi-Z Supernova Search Team Collaboration], 1998, Astron. J., 116, 1009.

[62] Riess, A.G., et al. [Hi-Z Supernova Search Team Collaboration], 1999, Astron. J., 117, 707.

[63] Saito S., Takada M., Taruya A., Phys. Rev. D 83, 043529 (2011).

[64] Samushia, L. et al. MNRAS, 439, 3504 (2013).

[65] Sánchez A. G. et al., MNRAS 425, 415 (2012).

[66] Scoccimarro R., PhRvD, 70, 083007 (2004).

[67] Seljak U., Slosar A. and McDonald P., JCAP 0610, 014 (2006).

[68] Seo H.-J., Eisenstein D. J., ApJ, 598, 720 (2003).

[69] Sheth R. K., Mo H. J., Tormen G., MNRAS, 323, 1 (2001).

[70] Smith R. E. et al. (The Virgo Consortium Collaboration), MNRAS, 341, 1311 (2003).

[71] Steinhardt, P. J., Wang, L. and Zlatev, I., 1999, Phys. Rev. D, 59, 123504 (1999).

[72] Thomas S. A., Abdalla F. B., Lahav O., Phys. Rev. Lett. 105, 031301 (2010).

[73] Tinker J. L., Robertson B.E., Kravtsov A.V., Klypin A., Warren M.S., Yepes G., Gottlöber S., ApJ, 724, 878 (2010).

[74] Tinker J. L., Weinberg D. H., Zheng Z., MNRAS, 368, 85 (2006).

[75] Verde, L. et al., MNRAS 335, 432 (2002).

[76] Wang L., Steinhardt P. J., ApJ, 508, 483 (1998).

[77] Wang, S., Haiman, Z., Hu, W., Khoury, J., May, M., Phys. Rev. Lett., 95, 011302 (2005)

[78] Yang X., Mo H. J., van den Bosch F. C., MNRAS, 339, 665, (2003).

[79] Zlatev, I., Wang, L. and Steinhardt, P. J., Phys. Rev. Lett., 82, 896 (1999).